Research Report
WSDOT Agreement T1874, Task 01

TPF-5(491) Super-Elastic Copper-Based and Iron-Based Shape Memory Alloys and Engineered Cementitious Composites for Extreme Events Resiliency

Interim Report - Phase 1

by

Bora Gencturk
Professor
University of Southern California

M. Saiid Saiidi
Professor
Infrastructure Innovation, LLC

Huanpeng Hong
Post-Doctoral Research Associate
University of Southern California

Washington State Department of Transportation

Technical Monitor
Amy Leland SE
State Bridge Design Engineer/Olympia, WA

Mustafa Mohamedali, PE, M.ASCE, PMP
Research Manager/Olympia, WA

Prepared for

The State of Washington
Department of Transportation
Roger Millar, Secretary

December 1, 2023

DISCLAIMER

The contents of this report reflect the views of the authors, who are responsible for the facts and the accuracy of the data presented herein. The contents do not necessarily reflect the official views or policies of the Washington State Department of Transportation, Federal Highway Administration or U.S. Department of Transportation [and/or another agency]. This report does not constitute a standard, specification, or regulation.

EXECUTIVE SUMMARY

Objectives

The objective of this report is to investigate the basic material properties of Fe-Mn-Si and Ni-Ti-Co shape memory alloys (SMA) and determine the feasibility of applying them in bridges subjected to harsh environmental conditions involving large climatic temperature variations, or earthquakes.

Background

Next-generation SMAs that have attracted research attention from the bridge engineering community include Cu-Al-Mn, Fe-Mn-Si and Ni-Ti-Co alloys. The Cu-Al-Mn SMA gained research attention due to its low-cycle fatigue stability, wide temperature range and low cost. The material behaviors of CAM SMA related to bridge applications have been comprehensively investigated by the authors and their research teams. The Fe-Mn-Si SMA (FeSMA) gained research attention due to its low cost, excellent shape memory effect and potential for use as post-tensioning elements. The Ni-Ti-Co SMA gained research attention due to its high strength, superelasticity and availability in large sizes. Due to the short history, studies on the mechanical behavior of FeSMA and Ni-Ti-Co SMA have been limited. The feasibility of applying these two materials in bridge columns subjected to earthquake loading and ambient temperature variations needs to be investigated.

Research Activities

Experimental characterization of FeSMA and Ni-Ti-Co SMA were performed. For FeSMA, monotonic, incremental cyclic and low-cycle fatigue tests were conducted before and after thermal actuation. Temperatures from -40 °C to 50 °C were evaluated. For Ni-Ti-Co SMA, incremental cyclic and low-cycle fatigue tests were performed at different temperatures from -

40 ℃ to 50 ℃. Comparisons with Ni-Ti and Cu-Al-Mn SMAs were also made. Moment-curvature analyses were performed on typical bridge columns reinforced with Ni-Ti-Co SMA. Comparisons with Ni-Ti and Cu-Al-Mn SMA as well as conventional reinforced concrete (RC) columns were also made.

Conclusions

It was found that FeSMA exhibits excellent deformability, cyclic actuation stability and low-cycle fatigue resistance under a wide range of temperatures from -40 ℃ to 50 ℃, which are advantageous for self-centering bridge applications. Ni-Ti-Co SMA was found to exhibit excellent superelastic behavior in terms of its flag-shaped stress-strain curves and strain recovery capacity under a wide range of temperatures. The low-cycle fatigue resistance of Ni-Ti-Co SMA was comparable to conventional Ni-Ti SMA at 23℃ and lower at 50℃. At -40 ℃, Ni-Ti SMA was found to completely lose its superelasticity while Ni-Ti-Co SMA showed excellent strain recovery and energy dissipation capacity up to 471 cycles, indicating the potential of applying Ni-Ti-Co SMA in bridges subjected to low temperatures. When applied in bridge columns, compared with columns reinforced with Ni-Ti or Cu-Al-Mn SMA, the moment capacity of Ni-Ti-Co columns was found to be higher, leading to a lower reinforcement ratio and smaller column diameter, for the same flexural capacity.

TABLE OF CONTENTS

LIST OF FIGURES

LIST OF TABLES

CHAPTER 1 Introduction

1.1 Introduction

Traditional designs of reinforced concrete (RC) bridge columns rely on the formation of column plastic hinges at predetermined locations in the bridges to absorb seismic energy and achieve a ductile seismic response. Although this design philosophy can effectively prevent collapse, the plastic hinge damage in the form of yielding of reinforcing bars accompanied by spalling and crushing of concrete during strong earthquakes can lead to large permanent drifts, which could seriously inhibit the traffic flow and cause indirect economic losses (Youssf et al. 2015). To alleviate the plastic hinge damage and permanent drift, possible strategies include using smart metals, damage-resistant cementitious materials, post-tensioning elements, and base isolation among others.

Shape memory alloys (SMAs) are considered for use in bridges due to their two special material properties, namely superelastic and shape memory effects. The superelastic effect allows SMAs to recover inelastic strain and dissipate energy upon unloading, and the shape memory effect allows SMAs to return to the original shape upon thermal stimulation, also referred to as actuation. The superelastic and shape memory effects of SMAs can be respectively used to provide strain recovery and post-tensioning in bridge columns, thereby, minimizing permanent drift. The feasibility of applying SMAs in bridge columns has been proven by previous experimental studies (Saiidi et al. 2009; Tazarv and Saiidi 2015).

Past research on SMAs mainly focused on the binary Ni-Ti alloy composition, which shows stable superelasticity and corrosion resistance. Nevertheless, for large-scale

applications, Ni-Ti SMAs still have the following limitations. First, the Ni-Ti SMAs are very expensive compared to steel and difficult to process (Hong et al. 2024a). Second, the martensitic transformation start temperature of Ni-Ti SMAs is normally higher than -25 ℃ (Zhang et al. 2008), which means they will lose superelasticity completely at very low temperatures. Third, the Ni-Ti SMAs are available commonly in thin wire forms. Manufacturing of Ni-Ti SMAs in large diameter with stable thermal-mechanical behavior is challenging and adds to the cost. The high cost, difficult machinability and limitation on operating temperature restrict the wide application of Ni-Ti SMAs in civil engineering. To overcome these limitations of conventional Ni-Ti SMAs, alternate materials are being studied.

Next-generation SMAs that have attracted attention from the bridge engineering community include Cu-Al-Mn, Ni-Ti-Co and Fe-Mn-Si alloys. The advantages of Cu-Al-Mn SMA mainly include low-cycle fatigue stability, superelasticity under a wide temperature range, ease of machinability, and relatively low cost (Gencturk and Saiidi 2022). The advantages of Ni-Ti-Co SMA mainly include high strength, superelasticity under a wide temperature range, and availability in large size. Cu-Al-Mn and Ni-Ti-Co SMAs are promising materials for bridge applications due to their superior superelasticity. The Fe-Mn-Si SMAs have received increasing research in the recent years due to their relatively low cost, shape memory effect and potential for use in post-tensioned concrete members (Cladera et al. 2014).

Previous research on Cu-Al-Mn, Ni-Ti-Co and Fe-Mn-Si SMA is briefly reviewed in the next section.

1.2 Previous research

Past research on Cu-Al-Mn SMA material properties was conducted mostly by the authors and their research teams. Through both experimental investigation and numerical simulations, the loading rate and temperature dependence (Gencturk et al. 2014), long-term corrosion behavior (Hong et al. 2022b), low-cycle fatigue resistance (Hong et al. 2022a), machinability characteristics (Hong et al. 2024a), headed coupling behavior with conventional steel rebar (Hong et al. 2024b), and cost efficiency (Gencturk and Saiidi 2022) of Cu-Al-Mn SMA have been investigated. The excellent loading rate stability up to 15 Hz and low-cycle fatigue resistance up to 50 k cycles of Cu-Al-Mn SMA are shown in Figure 1-1.

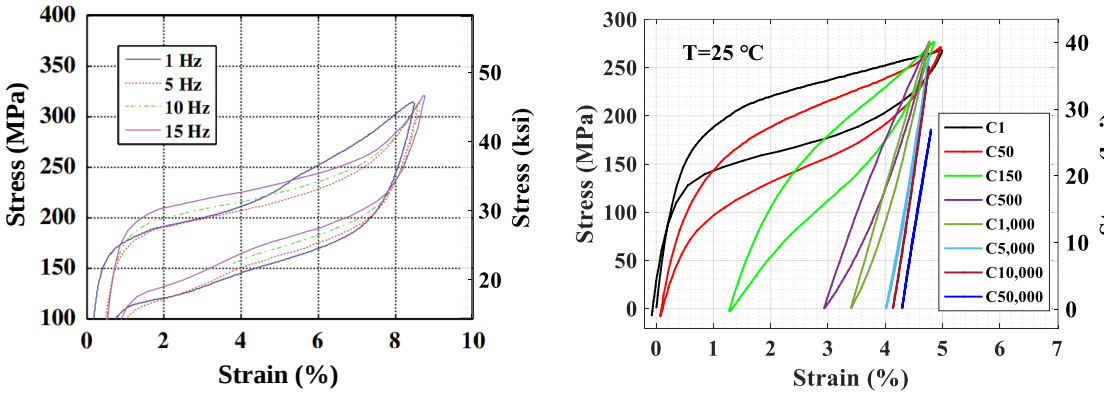

(a) (b)

Figure 1-1 Loading rate stability and low-cycle fatigue resistance of Cu-Al-Mn SMA: (a) redrawn from (Gencturk et al. 2014), and (b) redrawn from (Hong et al. 2022a).

Available data on material properties of Ni-Ti-Co SMA is very limited because the material is very new. Only some preliminary studies on thin wire Ni-Ti-Co SMA have been reported. According to Kishi et al. (2002), the addition of Cobalt (Co) increases the yield strength and decreases the martensitic transformation start temperature. Compared with conventional binary Ni-Ti SMAs, the yield strength of Ni-Ti-Co SMA can be more than

50% higher (Fasching et al. 2011; Manjeri et al. 2016). Large Ni-Ti-Co SMA round bars with diameters over 32 mm (1.26 in) have been recently developed. The availability in large bars indicates the possibility of using Ni-Ti-Co SMA in bridge columns. However, the mechanical behavior of large Ni-Ti-Co SMA has not been reported in literature.

Fe-Mn-Si SMA, also known as FeSMA, has received increasing attention for post-tensioning concrete structures (Shahverdi et al. 2018). In contrast to traditional approach using high strength steel tendons, the post-tensioning with FeSMA is not performed through application of an external load, but through their internal martensitic phase transformation via thermal stimulation, also known as "actuation". A diagram of the post-tensioning process with FeSMA is shown in Figure 1-2 (a). The advantage of using FeSMA is that the post-tensioning forces can be generated with no friction losses. Furthermore, since no heavy hydraulic devices are required, manpower and construction space can be saved. In addition to these advantages, FeSMA also has good machinability, weldability (Shahverdi et al. 2018) and low cost compared with other SMA compositions such as Ni-Ti-Nb alloys (Ma et al. 2020).

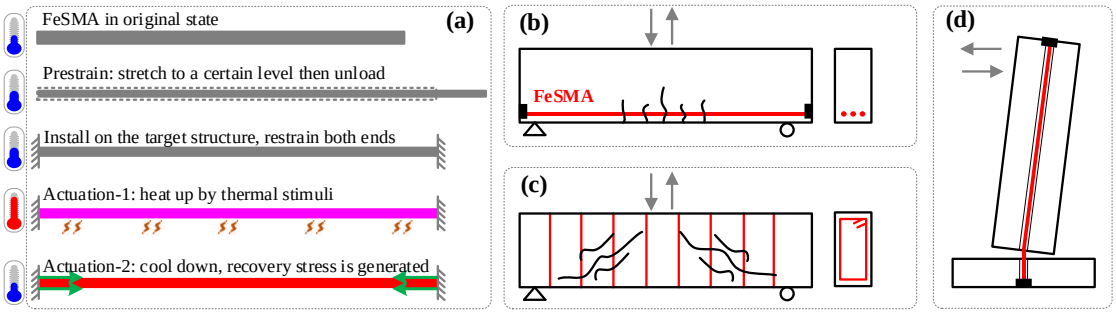

Figure 1-2 Diagrams of: (a) post-tensioning of FeSMA, (b) flexural and (c) shear strengthening of concrete beams, and (d) self-centering columns.

Extensive research has been conducted on using FeSMA to strengthen or repair concrete beams. Based on the role of prestraining forces in the beam, research can be

categorized into flexural and shear strengthening. In flexural strengthening, FeSMA is used to generate a post-tensioning force along the longitudinal direction of the beam, which is used to improve the stiffness and flexural capacity, see Figure 1-2 (b). Some examples of this application are presented in Schranz et al. (2021) and Vůjtěch et al. (2021). In shear strengthening, FeSMA is used to generate post-tensioning forces along the transverse direction of the beam. Transverse FeSMA hoops or strips are installed and actuated to improve the shear strength of beams, see Figure 1-2 (c). Some examples of this application are presented in Czaderski et al. (2021) and Cladera et al. (2020). In addition to existing studies on concrete beams, FeSMA also has potential for self-centering bridge columns in moderate and high seismic zones , see Figure 1-2 (c). Only two studies have been reported on the application of FeSMA in self-centering bridge columns (Raza et al. 2023, Vahedi et al. 2023).

When applying SMA bars in bridge columns, the earthquakes and ambient temperature changes may affect the mechanical behavior of SMA bars and thus threaten the safety of bridges. Specifically, the variation in ambient temperature for bridges in service can degrade the superelastic and shape memory effect of the SMA material. With regards to earthquake loading, a typical earthquake event may involve several load cycles, although the majority of the cycles will be with small amplitude (Shrestha et al. 2016). To ensure the bridges reinforced with SMAs remain operational after an earthquake, it is important for the SMA bars to maintain a stable low-cycle fatigue resistance without fracture.

Existing research on the low-cycle fatigue stability and dependence of mechanical behavior on temperature of FeSMA, Ni-Ti-Co and Cu-Al-Mn SMAs has been reviewed and the results are summarized in Figure 1-3. It is seen that research on low-cycle fatigue

behavior and temperature dependence of FeSMA and Ni-Ti-Co SMAs is very limited. Some high-cycle fatigue studies up to two million cycles were found on FeSMA, but only at room temperature and the strain amplitudes ranged only from 0.035% to 0.1%. Whereas for Ni-Ti-Co SMA, less than three studies were reported and they were all conducted by the manufacturer of the material, i.e., the SAES Smart Materials. More low-cycle fatigue tests on FeSMA and Ni-Ti-Co SMAs under different temperatures are still needed.

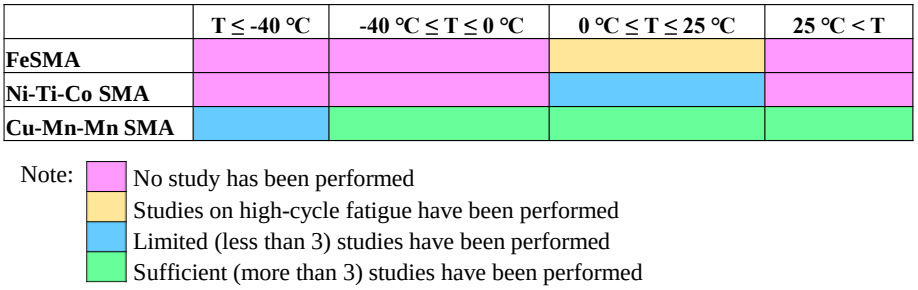

Figure 1-3 Summary of existing studies performed on low-cycle fatigue and temperature dependence of FeSMA, Ni-Ti-Co and Cu-Al-Mn SMAs.

1.3 Objectives and scope

The main objective of the study presented in this report was to investigate the material properties of FeSMA and Ni-Ti-Co SMA and determine the feasibility of applying them in bridges subjected to harsh environments. This study was the first phase of a broader study with the ultimate goal of determining alternative, cost-effective SMAs for application in bridges including developing design guidelines. The scope of Phase I was on the study of material characteristics consisting of Tasks 1 and 2. Specifically, Task 1: conduct low-cycle fatigue tests on FeSMA and Ni-Ti-Co SMAs at different temperatures. Task 2: conduct moment-curvature analysis of representative bridge columns reinforced with Ni-Ti-Co SMA.

1.4 Research Plan

The behavior of FeSMA before and after thermal activation was investigated. The effect of temperature on the strength, ductility and recovery strain was investigated for non-activated FeSMA. Monotonic and incremental cyclic loading were performed at -40℃, 23℃, and 50℃. The influence of temperature on the key mechanical properties of non-activated FeSMA, such as Young's modulus, yield strength, ductility and recovery strain were extracted and analyzed. For activated FeSMA, its actuation behavior was investigated through cyclic, low-cycle fatigue, and monotonic loadings. Different post-actuation temperatures (-40℃, 23℃, and 50℃), prestrain levels (4%, 15%, 20%, 25% and 30%) and low-cycle fatigue loading amplitudes (0.5% and 1%) were used. The influence of incremental cyclic loading and low-cycle fatigue loading on the deformability and actuation stress degradation of FeSMA was analyzed.

For Ni-Ti-Co SMA, both experimental characterization and numerical simulation were performed. In the experimental characterization, the effect of temperature on superelasticity, ductility, and low-cycle fatigue resistance was investigated and compared with properties of Ni-Ti and Cu-Al-Mn SMAs. Incremental cyclic loading was performed on these three SMAs at temperatures ranging from -40 ℃ to 50 ℃. Low-cycle fatigue loading with a constant strain amplitude of 5% was performed on Ni-Ti-Co and Ni-Ti SMAs at -40 ℃, 0 ℃, 23 ℃, and 50 ℃. The effect of low-cycle fatigue loading on the key superelastic properties, such as, Young's modulus, yield stress, damping ratio and recovery strain, of these two materials was extracted and analyzed.

In the numerical simulation part under Task 2, moment-curvature analysis using Open System for Earthquake Engineering Simulation (OpenSees) PEER (2000) was performed on typical bridge reinforced concrete (RC) round column sections that formed a benchmark.

Subsequently, SMA-reinforced ECC (engineered cementitious composite) versions were analyzed to match the plastic moment of RC sections. The amount of reinforcement and, when necessary, the column diameter were adjusted to obtain the target plastic moment. The influence of key parameters such as column section diameter, longitudinal reinforcement ratio and axial force ratio were evaluated in the moment-curvature analyses.

CHAPTER 2 EXPERIMENTAL CHARACTERIZATION OF FE-MN-SI SMA

2.1 Introduction

Fe-Mn-Si SMA, hereafter referred to as FeSMA, has great potential for post-tensioning bridge columns to provide self-centering. When using FeSMA to provide post-tensioning force, the material needs to be prestrained to a certain strain level prior to thermal activation (i.e., actuation). The prestrain levels as well as the variation of ambient temperatures can affect the behavior of FeSMA and thus threaten the safety or functionality of the bridge. However, the basic mechanical properties of FeSMA regarding these aspects have never been characterized.

To investigate the feasibility of applying FeSMA in self-centering bridge columns subjected to varying ambient temperatures and seismic loading conditions, comprehensive experimental characterization of FeSMA bars was conducted as presented in this chapter. The effect of temperature on the strength, ductility and recovery strain of FeSMA before actuation, as well as the effect of prestrain levels on the cyclic and low-cycle fatigue behavior of FeSMA after actuation were investigated.

2.2 Experimental program

2.2.1 Sample preparation

The composition of FeSMA used in this study is Fe–17Mn–5Si–10Cr–4Ni–1(V,C) (mass%), obtained from Re-fer AG, Switzerland. The as received material was 18 mm (0.7 in) diameter round bars. Cylindrical dog bone specimens with threads on both ends were prepared by machining. Metric threads with a major diameter of 18 mm (0.7 in) and a pitch of 1.5 mm (0.059 in) were machined on both ends of the sample; and the middle portion

was reduced to a diameter of 12.7 mm (0.5 inch), with a gauge length of 56 mm (2.2 in). The geometry of the specimen is shown in Figure 2-1.

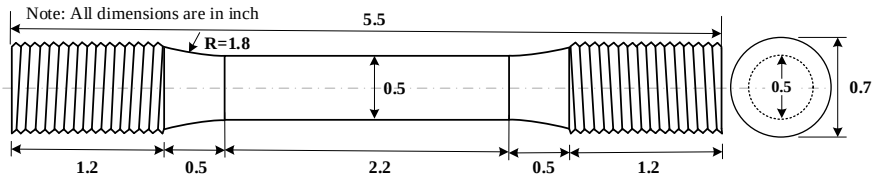

Figure 2-1 Dimensions of FeSMA samples.

2.2.2 Test setup

The test setup used in this study is shown in Figure 2-2. An MTS 370.5 dynamic servo-hydraulic frame was used to apply the load. An MTS 651.06E−04 environmental chamber was used along with the MTS load frame to house the specimens during testing. Two extension rods were used to connect the sample to hydraulic griping systems. A 50.8 mm (2 in) gauge length Epsilon extensometer (model number 3542-0200-100-LHT) was used to measure the strain. A BMS16HR-53 Mars Labs data acquisition system was used to record the data. A liquid nitrogen tank was used for low temperature tests and cooling during actuation, as shown in Figure 2-2 (a).

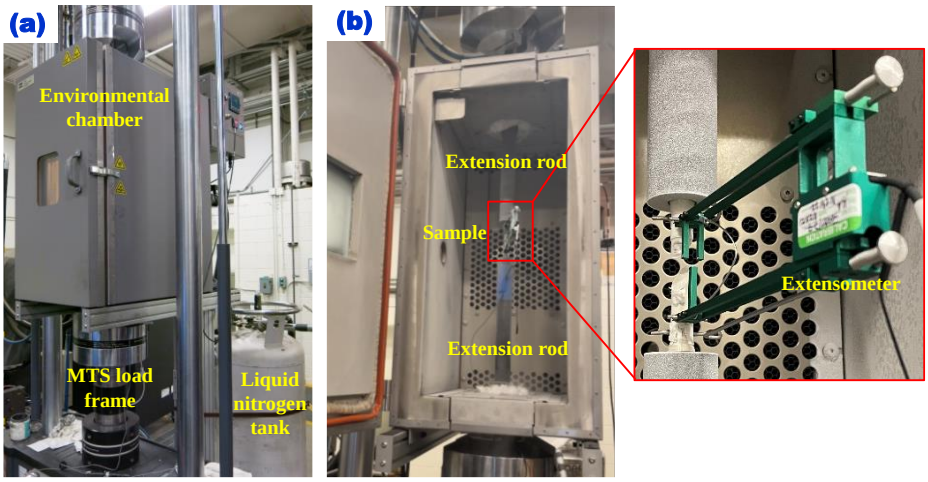

Figure 2-2 Test setup for characterization of FeSMA: (a) view from outside environmental chamber, and (b) inside view of environmental chamber.

2.2.3 Test methods

The behavior of FeSMA before and after actuation was investigated. For brevity, the FeSMA before actuation is referred to as non-activated FeSMA and the FeSMA after actuation is referred to as activated FeSMA hereafter. Different loading protocols and test methods were adopted for non-activated and activated FeSMA.

a) Non-activated FeSMA

Two loading protocols were adopted for non-activated FeSMA, namely monotonic loading and 1% strain incremental cyclic loading, see Figure 2-3. In the monotonic loading shown in Figure 2-3 (a), the sample was uniaxially stretched until fracture. In the incremental cyclic loading shown in Figure 2-3 (b), a 1% tensile strain incremental cyclic loading was applied until fracture. Extensometer controlled loading with a strain rate of 0.03% s^{-1} was adopted. Three different temperatures were investigated: specifically, -40 ℃, 23 ℃, and 50 ℃. When testing at different temperatures, the following procedures were adopted. First, install and place the sample in the chamber; then, adjust the chamber temperature to the target value, wait 40 minutes until the specimen temperature reaches equilibrium with the target temperature; finally, start the loading protocol.

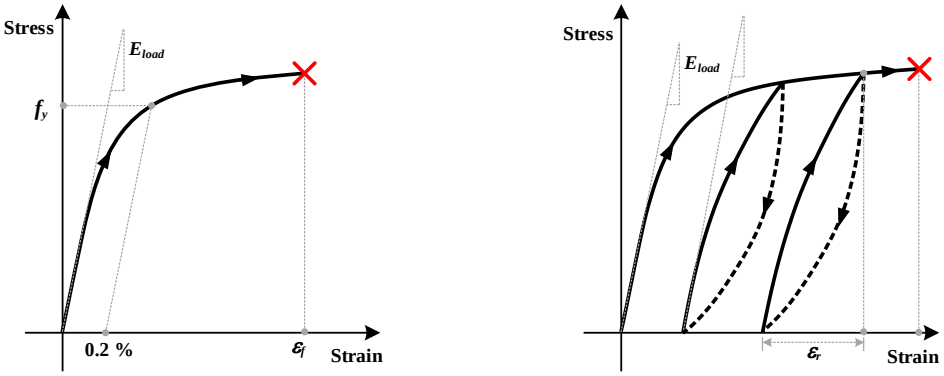

Figure 2-3 Schematic diagram of loading protocols and definition of key parameters: (a) monotonic loading, and (b) 1% strain incremental cyclic loading.

b) Activated FeSMA

The activated FeSMA samples were prestrained first and then activated by increasing the temperature. The FeSMA actuation process is shown in Figure 2-4 (a). First, at room temperature (T_0 = 23 ℃), the sample was stretched from point O to a certain strain level (point A) under extensometer control and then unloaded to zero force (point B) under force control. This process is so called "prestraining". For brevity, the strain level at point A is referred to as prestrain level hereafter. Second, the sample was stretched to 200 MPa (29 ksi, point C). This was done to avoid buckling when heating the sample under a constant strain, which causes thermal expansion and development of a compressive force. The third step was to keep the strain of the sample constant, raise the temperature in the chamber from 23 ℃ (point C) to 200 ℃ (point D), maintain this temperature for 15 mins, then cool down to a certain temperature (point E). The end of cooling temperature at point E is referred to as post-actuation temperature hereafter. The rate of both heating and cooling during actuation (point C to D to E) was 3 ℃/min.

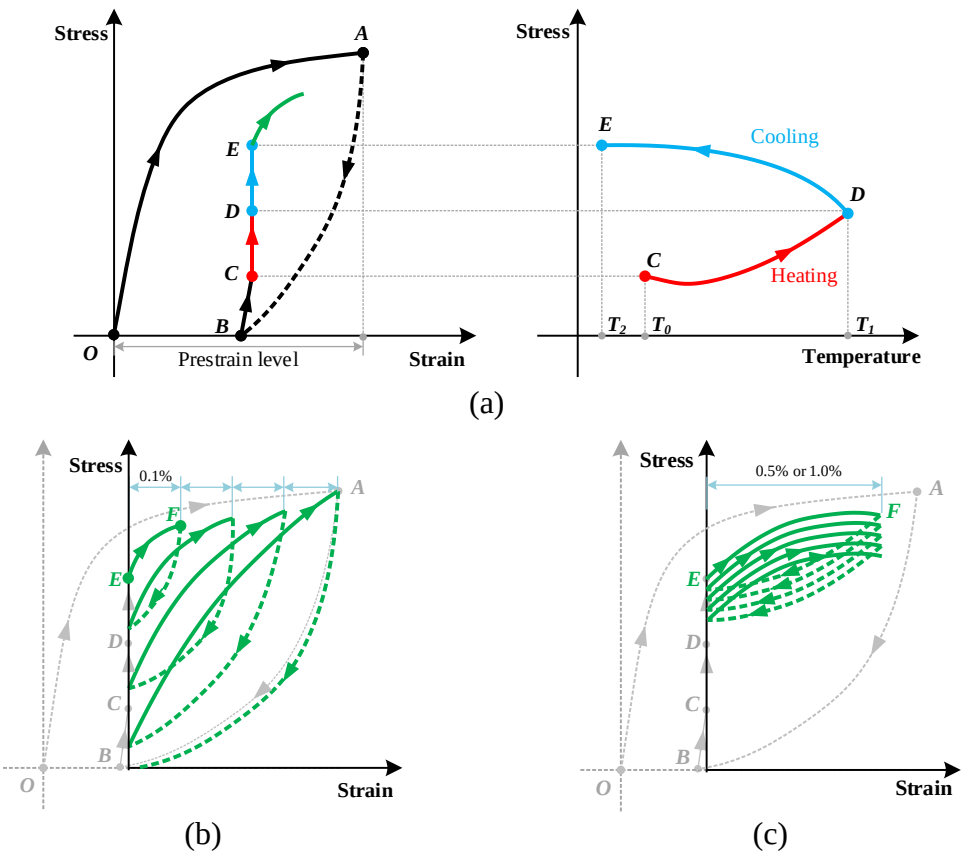

Figure 2-4 Schematic diagrams of: (a) actuation process of FeSMA, (b) incremental cyclic loading after actuation, and (c) low-cycle fatigue loading after actuation.

After the above actuation process, three different types of cyclic loading were investigated separately on the activated FeSMA samples, namely incremental cyclic loading, low-cycle fatigue loading and monotonic loading. In the incremental cyclic loading shown in Figure 2-4 (b), 0.1% strain incremental cyclic loading was applied on the activated FeSMA (from point E). In each cycle, the material was loaded and unloaded with respect to the end of actuation state, i.e., point E in Figure 2-4 (b). As the cyclic strain amplitude increased incrementally, the actuation stress decreased gradually upon unloading. The incremental cyclic loading was stopped when the actuation stress decreased to zero, as shown in Figure 2-4 (b). In the low-cycle fatigue loading shown in Figure 2-4 (c), constant strain cyclic loading was applied for 500 cycles. In each cycle, the material

was loaded to a constant strain amplitude with respect to the end of actuation state, i.e., point E in Figure 2-4 (c), then unloaded by the same constant strain amplitude. After incremental cyclic loading or low-cycle fatigue loading, the sample was monotonically stretched to failure. Extensometer controlled method with a strain rate of 0.03% s^{-1} was used for the loading and unloading process during the incremental cyclic loading, low-cycle fatigue loading, and monotonic loading on activated FeSMA.

A summary of the FeSMA samples used in this study and the test matrix are shown in Table 2-1. Sixteen FeSMA samples were tested, including six non-activated ones and ten activated ones. The labeling rule of the FeSMA samples is shown in Figure 2-5. The label of each sample consists of three parts: (1) activated or not; (2) the loading protocol applied after actuation; and (3) the post-actuation temperature. For example, A(4%)-C(0.1%)-23C means: it is an activated FeSMA sample, with a prestrain level of 4%; and after actuation, a 0.1% strain incremental cyclic loading was applied at 23 ℃.

Table 2-1 A summary of FeSMA samples and test matrix.

No.	Activated or not	Loading type	Prestrain	Fatigue amplitude	Post-actuation temperature	Sample
1	Non-activated	Monotonic	-	-	23 ℃	N-M-23C
2			-	-	50 ℃	N-M-50C
3			-	-	-40 ℃	N-M-m40C
4		1% incremental cyclic	-	-	23 ℃	N-C(1%)-23C
5			-	-	50 ℃	N-C(1%)-50C
6			-	-	-40 ℃	N-C(1%)-m40C
7	Activated	0.1% incremental cyclic	4%	-	23 ℃	A(4%)-C(0.1%)-23C
8			4%	-	50 ℃	A(4%)-C(0.1%)-50C
9			4%	-	-40 ℃	A(4%)-C(0.1%)-m40C
10			15%	-	23 ℃	A(15%)-C(0.1%)-23C
11			20%	-	23 ℃	A(20%)-C(0.1%)-23C
12			25%	-	23 ℃	A(25%)-C(0.1%)-23C
13			30%	-	23 ℃	A(30%)-C(0.1%)-23C
14		Low-cycle fatigue	15%	0.5%	23 ℃	A(15%)-F(0.5%)-23C
15			15%	1.0%	23 ℃	A(15%)-F(1.0%)-23C
16			20%	1.5%	23 ℃	A(20%)-F(1.0%)-23C

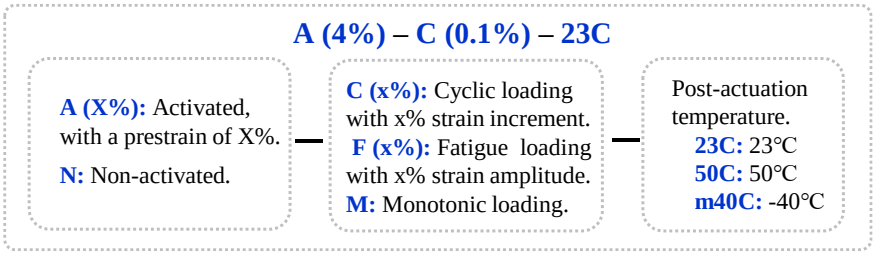

Figure 2-5 Labeling rule of FeSMA samples.

2.3 Results and discussion

2.3.1 Non-activated FeSMA

a) Monotonic behavior

The monotonic loading stress-strain curves of FeSMA under different temperatures are shown in Figure 2-6. The yield strength and ultimate strength of FeSMA increases as the temperature decreases, which is consistent with conventional reinforcing steels

(Montejo et al. 2008; Yan et al. 2023). The fracture strain of FeSMA at -40 ℃, 23 ℃ and 50 ℃ is 58%, 48% and 54%, respectively, indicating its excellent ductility under a wide range of temperatures. The fractured specimens are shown in Figure 2-7. The fracture location is indicated with red arrows. From the zoomed-in view shown in Figure 2-6 (b), the yield strength extracted by the 0.2% offset method (ASTM E8 2013) at -40 ℃, 23 ℃ and 50 ℃ is 532 MPa (77.2 ksi), 496 MPa (71.9 ksi) and 472 MPa (68.5 ksi), respectively. The Young's modulus of FeSMA is 168 GPa (24366 ksi), which is insensitive to temperature variation.

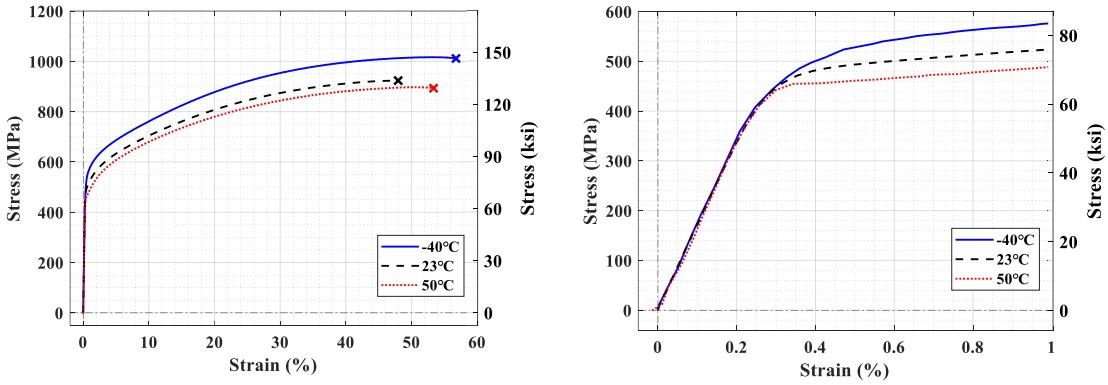

Figure 2-6 Monotonic loading stress-strain curves of FeSMA at different temperatures: (a) full view, and (b) zoomed-in view.

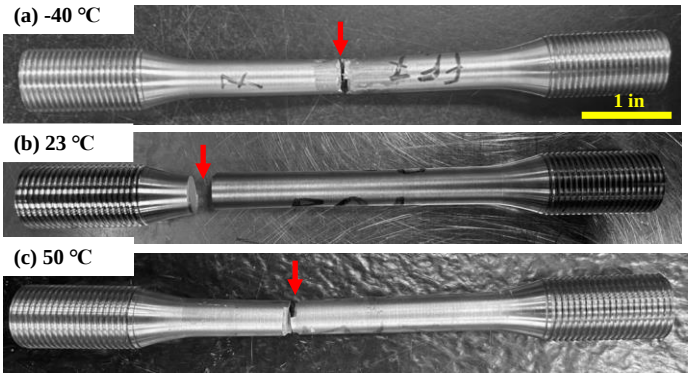

Figure 2-7 Photos of non-activated FeSMA samples after monotonic loading: (a) -40 ℃, (b) 23 ℃, and (c) 50 ℃.

b) Cyclic behavior

The cyclic loading stress-strain curves of FeSMA at different temperatures are shown in Figure 2-8. Under cyclic loading, the fracture strain of FeSMA at 23 ℃, -40 ℃ and 50 ℃ reached 27%, 45% and 40%, respectively. Such high fracture strains under incremental cyclic loading indicates the excellent deformability of FeSMA. The fractured specimens are shown in Figure 2-9. All three samples fractured near the edge of the gauge length and no obvious necking was observed. Like the monotonic loading results shown in Figure 2-6, FeSMA exhibited a lower fracture strain at 23℃.

The relationship between recovery strain ε_r, defined in Figure 2-3 (b), and the maximum applied strain is shown in Figure 2-10. It is seen that at all three temperatures, ε_r increases as the maximum applied strain increases. The trends at 23 ℃ and 50 ℃ are almost the same. The same is true at -40 ℃ up to 20% strain, but the increase is smaller afterwards. For example, ε_r at 5% maximum applied strain at -40 ℃, 23 ℃ and 50 ℃ is 0.86%, 0.83% and 0.92%, respectively. When the maximum applied strain was 25%, the ε_r at -40 ℃, 23 ℃ and 50 ℃ was 1.48%, 1.64% and 1.66%, respectively.

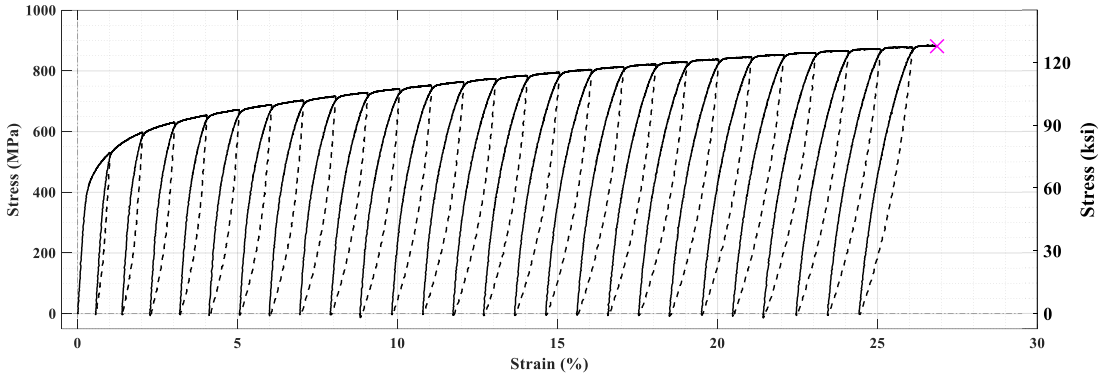

(a)

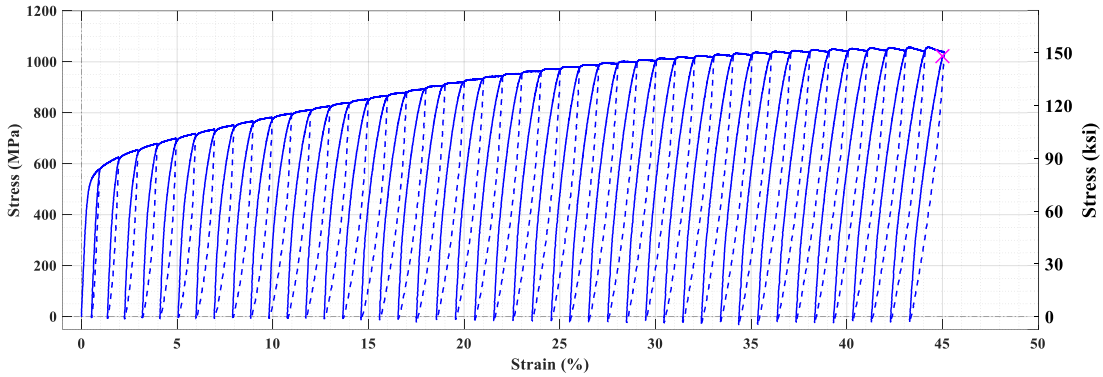

(b)

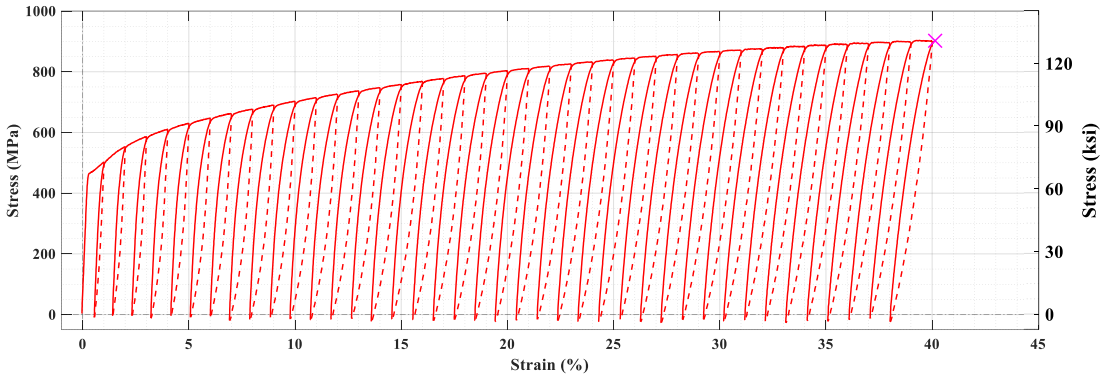

(c)

Figure 2-8 Incremental cyclic tests on FeSMA at different temperatures: (a) 23 ℃, (b) -40 ℃, and (c) 50 ℃.

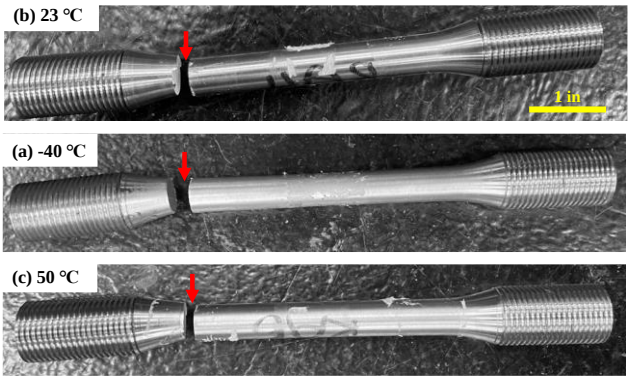

Figure 2-9 Photos of non-activated FeSMA samples after cyclic loading: (a) -40 ℃, (b) 23 ℃, and (c) 50 ℃.

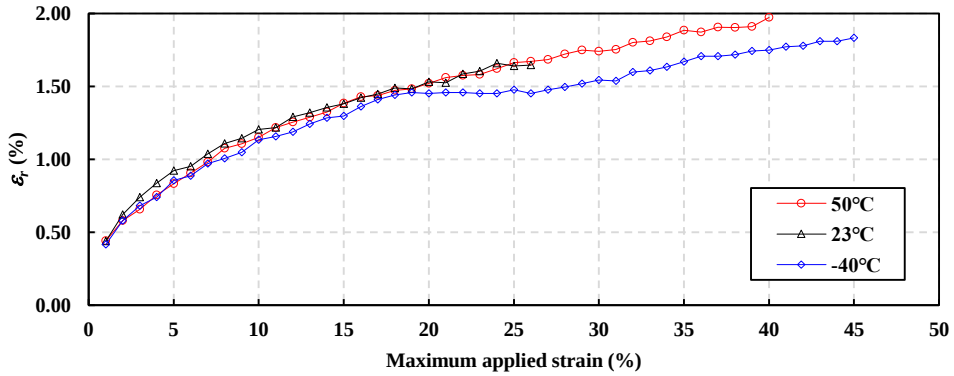

Figure 2-10 Variation of recovery strain with respect to maximum applied strain.

2.3.2 Activated FeSMA

a) Effect of post-actuation temperature

The results of incremental cyclic loading on FeSMA at different post-actuation temperatures are shown in Figure 2-11. The prestrain level of all these three samples was 4%. From Figure 2-11, it is seen that the initial actuation stress, i.e., the stress at point E shown in Figure 2-4 (b), decreases as the post-actuation temperature increases. Specifically, when the post-actuation temperatures are -40 ℃, 23 ℃ and 50 ℃, the actuation stresses are 521 MPa (74.3 ksi), 402 MPa (58.3 ksi), and 188 MPa (27.3 ksi), respectively.

The reason why FeSMA exhibits a higher actuation stress at a lower post-actuation temperature is that the actuation stress is mainly developed during the cooling process, as shown in Figure 2-4 (a), point D to E. During cooling, both phase transformation and thermal cooling shorten the sample; thereby, generating the actuation stress. A low post-actuation temperature means the cooling ends at a lower target temperature (at point E in Figure 2-4 (a)), therefore, the phase transformation together with the thermal shrinkage can be fully developed, leading to a higher actuation stress. Regarding the actuation stress degradation with respect to incremental cyclic loadings, it is seen from Figure 2-11 that, at 23 ℃, -40 ℃ and 50 ℃, the actuation stress decreases to zero when the cyclic loading amplitude reaches 0.82%, 0.80% and 0.73%, respectively. The strain amplitudes when actuation stress disappear are consistent with the recovery strain shown in Figure 2-10.

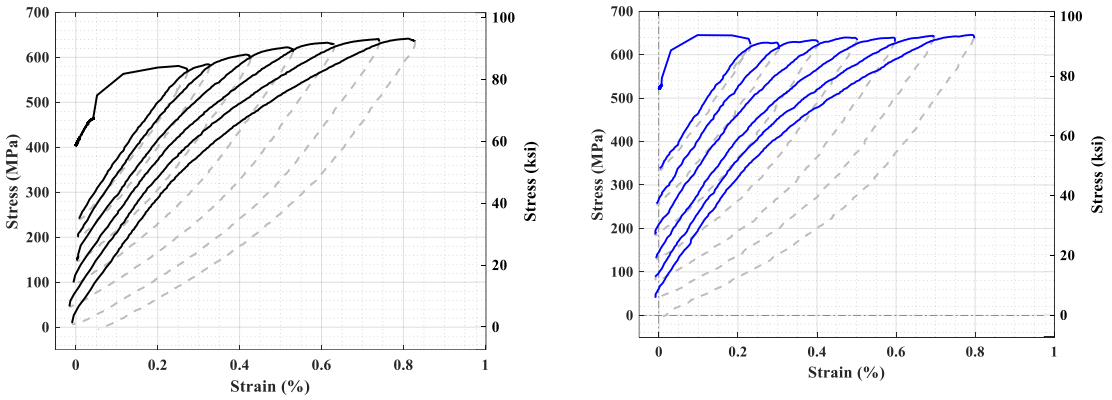

(a) (b)

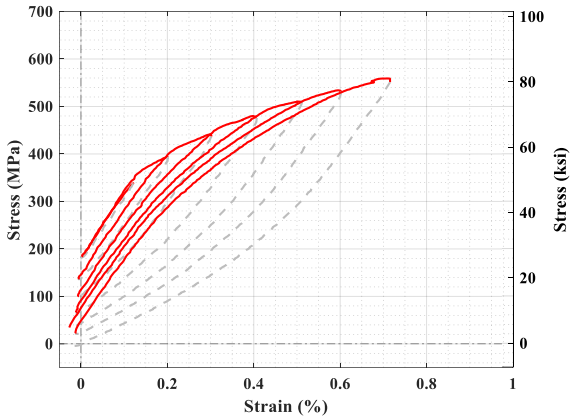

(c)

Figure 2-11 Results of incremental cyclic loading tests on FeSMA under different post-actuation temperatures: (a) 23 ℃, A(4%)-C(0.1%)-23C, (b) -40 ℃, A(4%)-C(0.1%)-m40C, and (c) 50 ℃, A(4%)-C(0.1%)-50C.

b) Effect of prestrain level

FeSMA is prestrained to only 4% prior to actuation in most of past studies and applications. This prestrain level is sufficient when FeSMA is used to strengthen existing beams in flexure or shear. In the research reported by Lee et al. (2013) and Shahverdi et al. (2018), the actuation stress of FeSMA shows an apparent increase when the prestrain level increases up to 2%. A prestrain level exceeding 4% has negligible influence on the actuation stress magnitude. The magnitude of actuation stress is the main target when strengthening or repairing existing structures. However, for self-centering bridge column applications, the prestressing force in the FeSMA bars decreases as the FeSMA strain increases under seismic loads. To maintain a reasonable level of recentering force in the column, it is necessary to increase the prestrain level beyond 4%.

In Figure 2-10, it is seen that the recovery of FeSMA increases as the maximum applied strain increases. Specifically, at room temperature 23 ℃, when the maximum applied strain is tripled from 5% to 15%, the recovery strain changes from 0.92% to 1.36%,

increased by 48%. Therefore, a prestrain level of 4% does not take full advantage of the strain recovery capacity of FeSMA. A larger prestrain level needs to be explored to fully utilize the strain recovery capacity and ensure recentering of the bridge columns. To determine the effect of prestrain level on strain recovery of FeSMA, prestrain levels of 15%, 20%, 25% and 30% were studied.

The results of cyclic loading on FeSMA at different prestrain levels are shown in Figure 2-12. The post-actuation temperature of these samples were all 23 ℃. From Figure 2-12 (a) to (c), it is seen that, at prestrain levels of 15%, 20% and 25%, the actuation stress decreases to zero when the cyclic loading amplitude reaches 1.3%, 1.5% and 1.7%, respectively. Compared with the results at 4% prestrain level shown in Figure 2-12 (a), it is seen that raising the prestrain level increases the post-actuation strain amplitude at which the actuation stress (that provides recentering forces) reduces to zero.

This is an important finding for self-centering bridge column applications, because this means that, by increasing the prestrain level of FeSMA, the columns can withstand greater seismic deformations without losing the recentering force. However, the prestrain level cannot be too high because it could fracture the bar under seismic loads. As shown in Figure 2-12 (d), when the prestrain level was 30%, although the actuation stress did not reduce to zero, the sample fractured at 1.2% strain (total FeSMA strain of 31.2%) during the cyclic loading. This means the 30% prestrain level is too high and significantly reduces the post-actuation deformability of FeSMA. The sample fractured at 30% prestrain will be presented later in Figure 2-14 (a).

The initial actuation stress for 20% prestrain sample shown in Figure 2-12 (b) was higher than the other three samples because using the current extensometer controlled

method, the response of the FeSMA during actuation (when a constant strain was required on the sample) was very sensitive small changes in the extensometer reading. However, since these tests were aimed at studying the effect of post-actuation force degradation, the validity of the results was not affected by this initial stress level. The 20% prestrain sample shown Figure 2-12 (b) lost the actuation stress when cyclic loading amplitude reaches 1.5%, which is still valid and consistent with the recovery strain value shown in Figure 2-10.

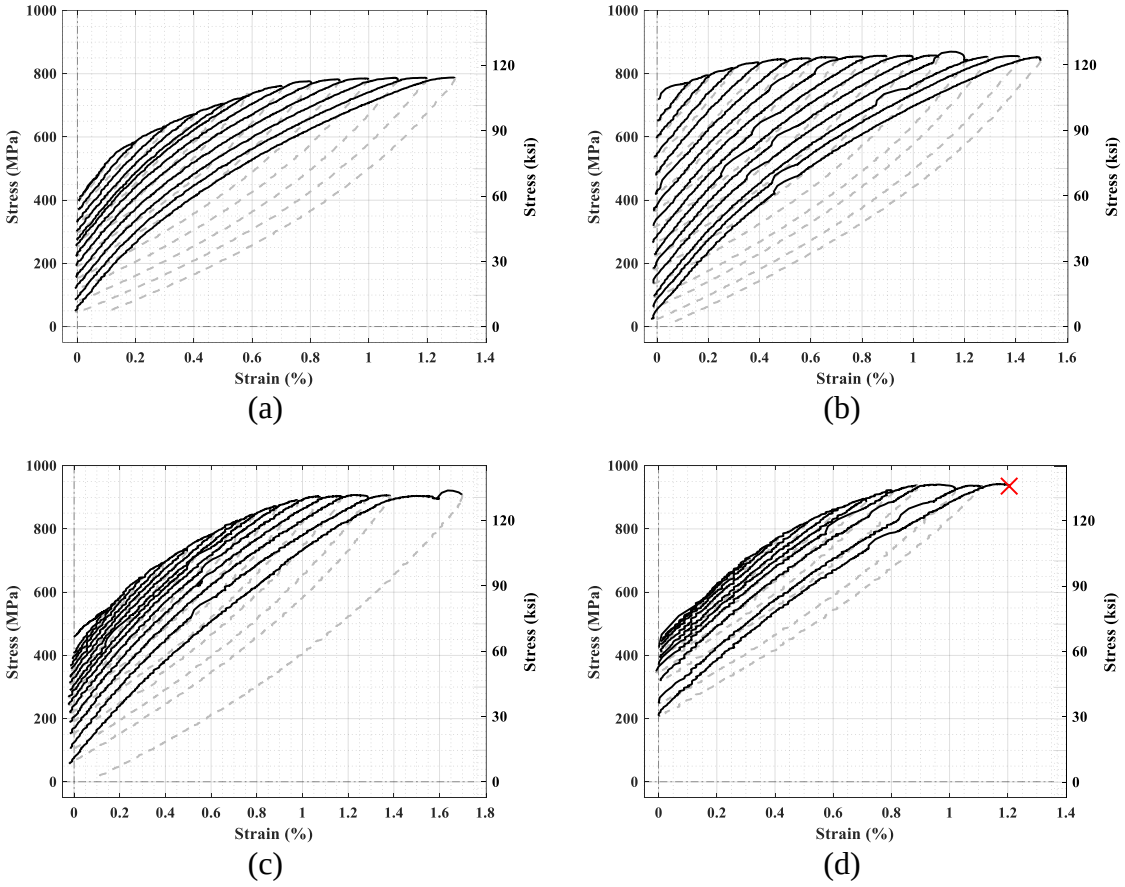

Figure 2-12 Results of incremental cyclic loading on FeSMA at different prestrain levels: (a) 15%, A(15%)-C(0.1%)-23C, (b) 20%, A(20%)-C(0.1%)-23C, (c) 25%, A(25%)-C(0.1%)-23C, and (d) 30%, A(30%)-C(0.1%)-23C.

The monotonic test results of sample with 15%, 20%, and 25% prestrain are shown in Figure 2-13. At prestrain levels of 15%, 20% and 25%, the fracture strain is 25.8%, 16.1%,

and 15.4%, respectively. The fractured specimens are shown in Figure 2-14 (b) to (d). The fracture of FeSMA sample with 20% prestrain occurred outside of the gauge length, indicating its true elongation was even larger than 16.1%. From the monotonic test results, it is confirmed that when increasing the prestrain level to 25%, the FeSMA still has a reserve post-actuation deformability of more than 15%, which is on the same order of magnitude of a pristine deformed steel reinforcing bar. However, in order to avoid the possible fracture of FeSMA bars, a prestrain level of 15% or 20% is suggested for the practical applications.

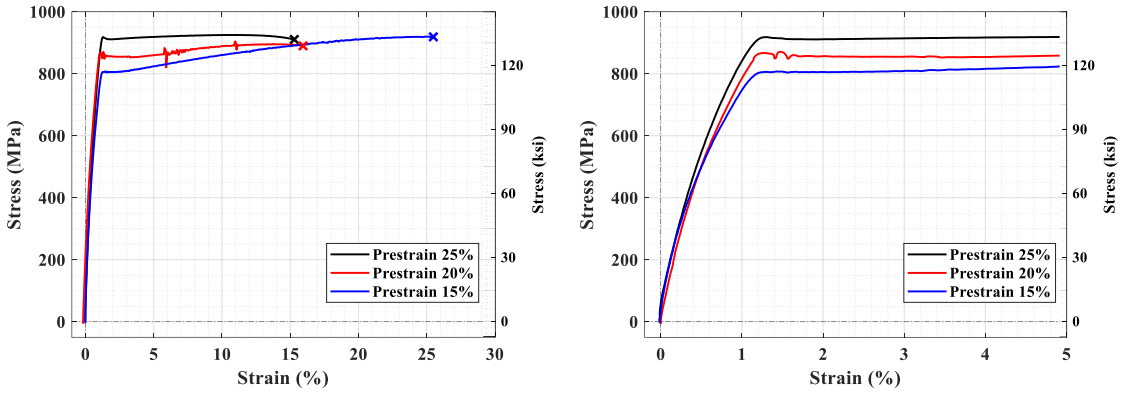

Figure 2-13 Results of monotonic loading tests on FeSMA after incremental cyclic loading: (a) full view, and (b) zoomed-in view.

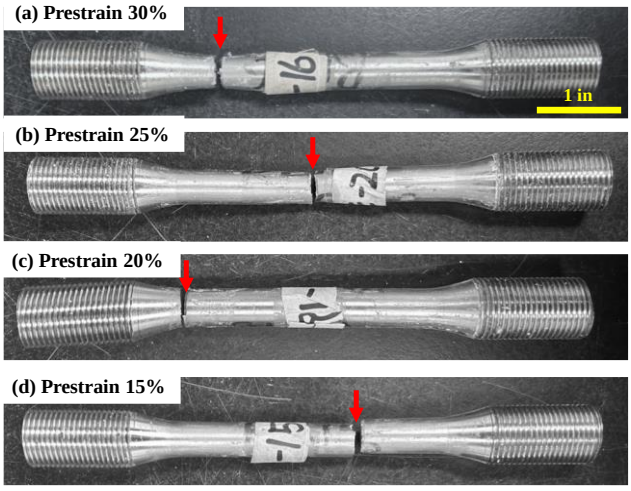

Figure 2-14 Photos of activated FeSMA samples after incremental cyclic and subsequent monotonic loadings: (a) prestrain 30%, (b) prestrain 25%, (c) prestrain 20%, and (d) prestrain 15%.

c) Low-cycle fatigue resistance

Based on the cyclic and subsequent monotonic loading test results, prestrain levels of 15% and 20% were used to conduct low-cycle fatigue tests on FeSMA. To simulate the seismic loading condition when applying FeSMA in self-centering bridge columns, two strain amplitudes: 0.5% and 1.0% were applied. According to Motaref (2011a), when the drift ratio of a self-centering precast segmental column reaches 10%, the strain of post-tensioning tendons is around 0.5%. Raza et al. (2023) performed quasi-static cyclic loading on RC columns strengthened with FeSMA bars and found that when the drift ratio of the column reaches 5%, the maximum strain of FeSMA was around 0.8%. Therefore, it is assumed that the low-cycle fatigue strain amplitudes of 0.5% and 1.0% cover most of the earthquake excitations when applying FeSMA in self-centering bridge columns.

The low-cycle fatigue test results of FeSMA are shown in Figure 2-15. All specimens were tested at room temperature. The specimens in Figure 2-15 (a) and (b) were prestrained to 15% and the one in Figure 2-15 (c) was prestrained to 20%. Overall, it was found that

FeSMA exhibited excellent low-cycle fatigue resistance in terms of actuation stress and energy dissipation stability up to 500 cycles. Specifically, from Figure 2-15 (a) and (b), it is seen that under a prestrain level of 15%, when the fatigue amplitude was 0.5%, the hysteresis loop of FeSMA showed almost no degradation after 500 cycles: the stress-strain curves at cycle 5, 100 and 500 were almost the same. When the fatigue amplitude was 1.0%, the degradation of the hysteresis loop was still negligible; after unloading, the residual actuation stress was around 1/2 of that under 0.5% fatigue; besides, the hysteresis loop narrowed slightly under higher fatigue amplitude. From Figure 2-15 (c), it is seen that when the prestrain level was increased to 20%, the hysteresis loops were still stable with no degradation. Compared with Figure 2-15 (b), it is noted that increasing the prestrain level to 20% led to slightly narrower hysteresis loops.

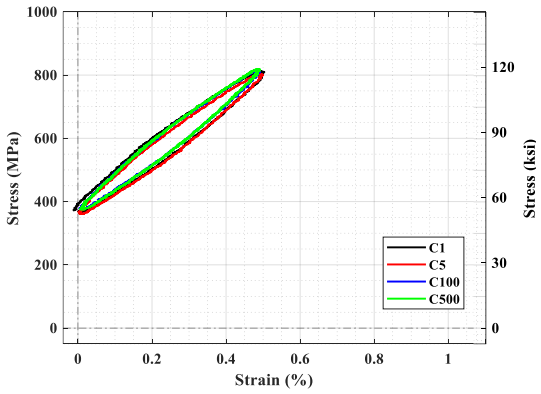

(a)

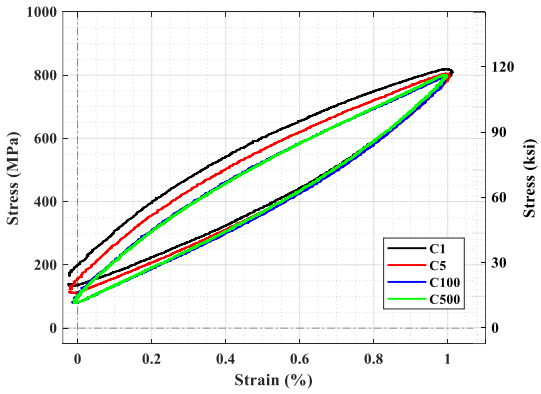

(b)

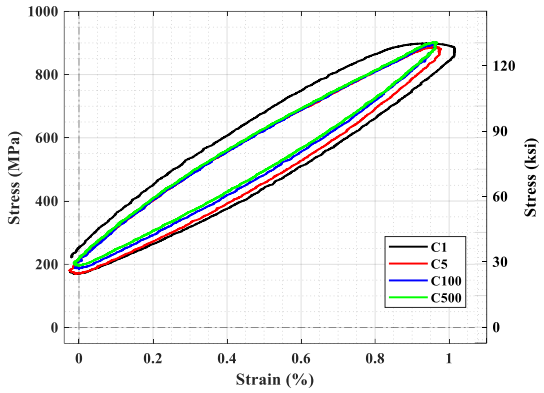

(c)

Figure 2-15 Results of low-cycle fatigue tests on FeSMA: (a) prestrain 15% & fatigue 0.5%, A(15%)-F(0.5%)-23C, (b) prestrain 15% & fatigue 1.0%, A(15%)-F(1.0%)-23C, and (c) prestrain 20% & fatigue 1.0%, A(20%)-F(1.0%)-23C.
Note: 'C1' means cycle 1.

After low-cycle fatigue loading, monotonic tensile loading was performed on FeSMA until failure. The results of monotonic loading test are shown in Figure 2-16. The fracture strain of samples with: prestrain 20% & fatigue 1%, prestrain 15% & fatigue 0.5%, and prestrain 15% & fatigue 1.0%, was 19.8%, 13.7% and 9.3%, respectively. From Figure 2-16 (b), it is seen that after 500 cycles of low-cycle fatigue loading, the sample with 20% prestrain level showed higher strength and Young's modulus during the monotonic loading. It is worth noting that even at a high prestrain level of 20%, after 500 cycles of 1.0% strain low-cycle fatigue loading, the sample still showed excellent ductility with a fracture strain exceeding 9%. The fractured specimens are shown in Figure 2-14.

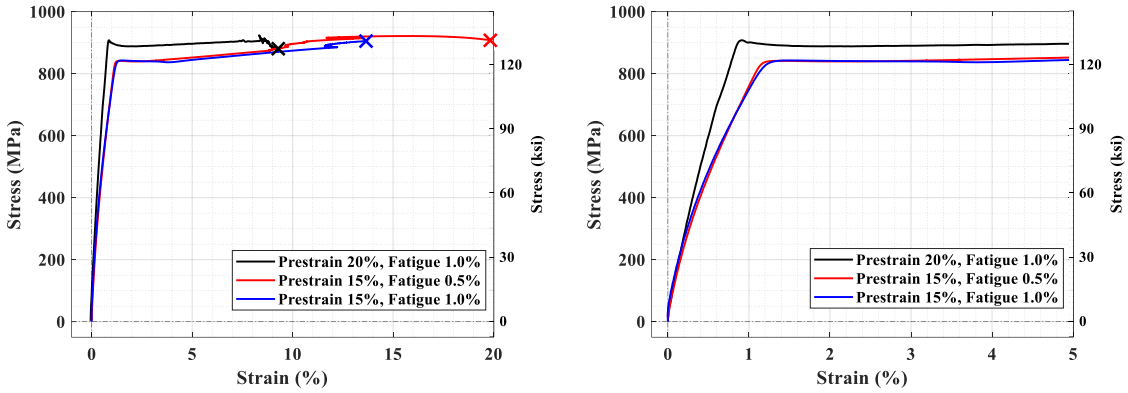

Figure 2-16 Results of monotonic loading tests on FeSMA after low-cycle fatigue loading: (a) full view, and (b) zoomed-in view.

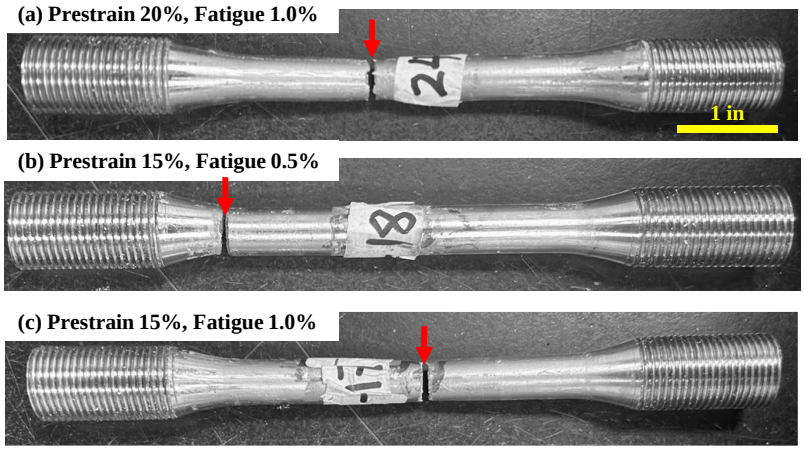

Figure 2-17 Photos of activated FeSMA samples after low-cycle fatigue and subsequent monotonic loading: (a) prestrain 20% and fatigue 1.0%, (b) prestrain 15% and fatigue 0.5%, and (c) prestrain 15% and fatigue 1.0%.

2.4 Summary

The non-activated FeSMA was found to have excellent ductility under a wide range of ambient temperatures from -40 ℃ to 50 ℃. Under both monotonic and cyclic loading, the fracture strain at all three temperatures were over 25% and the maximum total strain reached 58%. The yield strength and ultimate strength of non-activated FeSMA increased as the ambient temperature decreased, which is consistent with conventional reinforcing

steel. The recovery strain of non-activated FeSMA increased significantly with the increasing maximum applied strain or maximum applied stress.

Activated FeSMA exhibited excellent post-actuation deformability and low-cycle fatigue resistance, which are advantageous for self-centering bridge columns under seismic loads. Increasing the prestrain level increased the post-actuation strain amplitude before the actuation stress reduced to zero. Specifically, at the prestrain levels of 15%, 20% and 25%, the actuation stress decreased to zero when the cyclic loading amplitude reached 1.3%, 1.5% and 1.7%. A 60% to 110% increase compared to the bars prestrained to 4% strain (commonly used in past research). At a fatigue loading amplitude of 0.5% and a prestrain level of 15%, the hysteresis loops of FeSMA remained stable, and the fracture strain after subsequent monotonic loading exceeded 19%.

CHAPTER 3 EXPERIMENTAL CHARACTERIZATION OF NI-TI-CO SMA

3.1 Introduction

Superelastic Ni-Ti-Co SMA is potentially attractive for application in bridge columns due to its high strength and availability in large diameters of up to 32 mm (1.26 in). However, due to the short research history, only very limited publications on thin wire-shaped Ni-Ti-Co SMA are available, and the basic mechanical properties of large size Ni-Ti-Co SMA have not been reported. Before application of large size Ni-Ti-Co SMA into bridges subjected to extreme environments, it is necessary to fully understand the superelasticity, ductility, temperature dependence and low-cycle fatigue resistance of this new alloy composition.

Here, investigations on the cyclic and low-cycle fatigue behavior of Ni-Ti-Co SMA bars under different temperatures were reported. Comparisons with Cu-Al-Mn SMA and conventional Ni-Ti SMA were also made. Temperatures considered include room temperature 23 ℃, low temperatures of -40 ℃ and -20 ℃, and a high temperature of 50 ℃. The effect of cyclic and low-cycle fatigue loading on the key superelastic properties of Ni-Ti-Co and Ni-Ti SMAs was extracted and analyzed.

3.2 Experimental program

3.2.1 Sample preparation

Three types of materials were included in this study, namely Ni-Ti-Co SMA, Ni-Ti SMA and single crystal Cu-Al-Mn SMA. Both Ni-Ti-Co and Ni-Ti SMAs were obtained from SAES Smart Materials. The composition of single crystal Cu-Al-Mn SMA was Cu-8.38Al-11.32Mn (wt. %), obtained from Furukawa Techno Material Co., Ltd. The as

received dimensions of three SMAs were as follows. The Ni-Ti-Co SMAs were received as round bars with 32 mm (1.26 in) diameter and approximately 1.8 m (5.9 ft) length. The Ni-Ti SMAs were received as round bars with 27.2 mm (1.07 in) diameter and approximately 1.9 m (6.2 ft) length. The Cu-Al-Mn SMAs were received as round bars with 20 mm (0.79 in) diameter and 30 cm (1.0 ft) length.

The dimensions of Ni-Ti-Co, Ni-Ti and Cu-Al-Mn SMA samples used in this study are shown in Figure 3-1. To compare Ni-Ti-Co, Ni-Ti and Cu-Al-Mn SMAs under same conditions, all three materials were machined into cylindrical dog-bone samples with the same effective diameter of 12.7 mm (1/2 in), and with the same end thread of M18-1.5 (a major diameter of 0.7 in and a pitch of 0.059 in). The thread length of Ni-Ti-Co and Ni-Ti samples was 5 mm (0.2 in) longer than that of Cu-Al-Mn SMA samples considering their higher strength. The following machining methods were adopted. For Cu-Al-Mn SMA, only conventional computer numerical control (CNC) machining was used for the sample preparation. Whereas for Ni-Ti-Co and Ni-Ti SMA, due to their difficult machinability, both conventional CNC machining and non-conventional machining techniques were used. First, they were cut into short pieces with a water jet; then, electro discharge machining (EDM) was used to reduce them into round bars with a diameter of 18 mm (0.7 in); finally, conventional CNC machining was used to form the dog bone shape and add threads on both ends. After machining all Ni-Ti-Co and Ni-Ti SMA samples into designed shape, they were heat treated to stabilize their martensitic transformation. The heat treatment temperature was 375 °C with a duration of 40 mins.

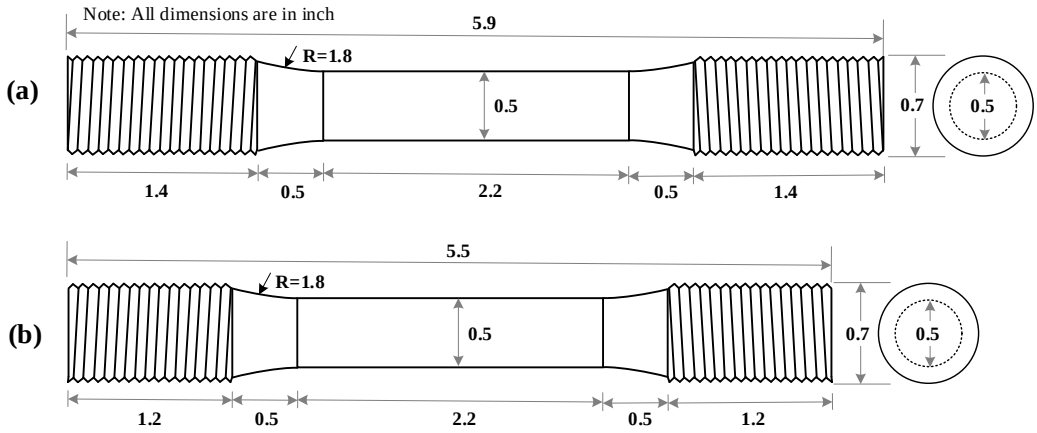

Figure 3-1 Dimensions of (a) Ni-Ti-Co and Ni-Ti, and (b) Cu-Al-Mn SMA specimens.

3.2.2 Test methods

The test set up used in this study was the same as previously mentioned in Chapter 2 and is not repeated here. Both cyclic tests and low-cycle fatigue tests under different temperatures were performed.

a) Cyclic tests

The cyclic tests were intended to understand the superelastic behavior and temperature dependence of Ni-Ti-Co SMA in comparison with Ni-Ti and Cu-Al-Mn SMA. Two different loading protocols (LPs) were considered in the cyclic tests. The LP-1 is 1% strain incremental cyclic loading until failure at room temperature, 23 ℃. After reaching the target strain at each cycle, the sample was unloaded to near-zero force under force control, then the next increment was initiated. The LP-2 is 1% strain incremental cyclic loading until 5% under different temperatures. The following temperatures were used for Ni-Ti-Co SMA: -40 ℃, -20 ℃, 0 ℃, 23 ℃ and 50 ℃. The test temperatures used for Ni-Ti SMA were -20 ℃, 0 ℃, 23 ℃, and 50 ℃. The test temperatures for Cu-Al-Mn SMA were -40 ℃, 23 ℃ and 50 ℃. The low temperatures for the three SMA types were not the same because Based on the authors' previous work, Cu-Al-Mn SMA is known to have

stable superelasticity at temperatures as low as -40°C (Hong et al. 2022a). The same for Ni-Ti-Co and Ni-Ti SMAs is however unknown. Therefore, test temperatures for Ni-Ti-Co and Ni-Ti SMA were gradually decreased until superelasticity disappeared to determine their low temperature limit. Loading with a strain rate of 0.08% s^{-1} was adopted for both LP-1 and LP-2.

b) Low-cycle fatigue tests

Ni-Ti-Co and Ni-Ti SMA samples were subject to low cycle fatigue tests at a constant amplitude of 5% until fracture. In each cycle, the loading was performed under extensometer control until 5% strain; then the sample was unloaded to near-zero force under force control. The strain rate was 0.08% s^{-1}. The Cu-Al-Mn SMA was not considered in the fatigue tests because its low-cycle fatigue behavior at temperatures ranging from -40 ℃ to 50 ℃ has been comprehensively investigated in the authors' previous work (Hong et al. 2022a).

A summary of low-cycle fatigue tests on Ni-Ti-Co and Ni-Ti SMA is provided in Table 3-1. In Table 3-1, 'Training' means 1% incremental cyclic loading until 5%; 'Fatigue' means 5% constant strain low-cycle fatigue loading. Training is a commonly used approach to stabilize the martensitic transformation of SMAs (Gencturk et al. 2014). Three temperatures were performed for Ni-Ti-Co SMA, namely room temperature 23 ℃, high temperature 50 ℃ and low temperature -40 ℃. Whereas for Ni-Ti SMA, it is found that when temperature was -20 ℃, the material lost superelasticity completely. Therefore, the low temperature performed for Ni-Ti SMA was changed to 0 ℃. It is noted that the low-cycle fatigue loading on NiTi-2 at 0℃ was terminated at 800 cycles when a stabilized stress-

strain response was observed. Except for this sample, all the other Ni-Ti-Co and Ni-Ti SMA samples were tested until fracture.

Table 3-1 Summary of low-cycle fatigue tests on Ni-Ti-Co and Ni-Ti SMA.

Material	Sample label	Temperature	Loading protocol
Ni-Ti-Co SMA	NiTiCo-1	Room temperature (23 ℃)	Fatigue
	NiTiCo-2	Low temperature (-40 ℃)	Fatigue
	NiTiCo-3	High temperature (50 ℃)	Fatigue
Ni-Ti SMA	NiTi-1	Room temperature (23 ℃)	Fatigue
	NiTi-2	Low temperature (0 ℃)	Fatigue
	NiTi-3	High temperature (50 ℃)	Training + Fatigue

After obtaining the stress-strain curves, eight mechanical properties were extracted and analyzed, namely, Young's modulus, E_{load}, elastic modulus after yielding, E_{load2}, maximum stress, σ_{max}, yield stress, σ_y, damping ratio, δ_R, maximum strain, ε_{max}, residual strain, ε_{resi}, and recovery strain, ε_{reco}. These parameters are shown in Figure 3-2.

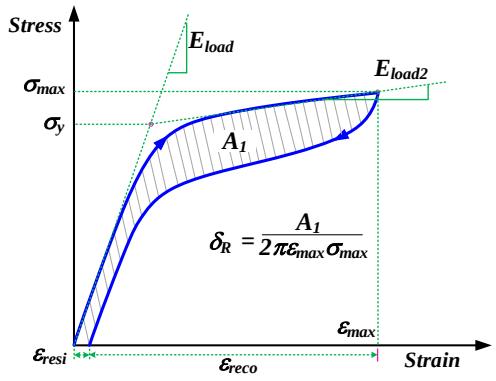

Figure 3-2 Definitions of superelastic parameters.

3.3 Results and discussion

3.3.1 Cyclic tests

a) Superelasticity and ductility

The results of 1% strain incremental cyclic loading until failure on Ni-Ti-Co and Ni-Ti SMA at 23 °C are shown in Figure 3-3. Ideal flag shape stress-strain curves are observed for Ni-Ti-Co SMA up to 7% strain. Strain hardening (after the martensitic transformation finish point) was observed at around 5%. The sample fractured during the 8th cycle when the strain was 8% (as marked by the red cross). The Young's modulus, E_{load}, and yield stress, σ_y, of Ni-Ti-Co SMA at 23 °C was 40 GPa (5801.5 ksi) and 631 MPa (91.5 ksi), respectively. In Figure 3-3 (b), an ideal flag shaped stress-strain curve of Ni-Ti SMA was observed up to 7% strain, which was similar to that of Ni-Ti-Co SMA. The Ni-Ti SMA fractured when the strain reached 8.5%. The E_{load} and σ_y of Ni-Ti SMA at 23 °C were 35 GPa (5656.5 ksi) and 396 MPa (57.4 ksi), respectively, which were lower than that of Ni-Ti-Co SMA.

The photos of fractured Ni-Ti-Co and Ni-Ti SMA samples are shown in Figure 3-4. The Ni-Ti-Co SMA fractured and produced a small fragment, see Figure 3-4 (a). For NiTi SMA, see Figure 3-4 (b), the failure occurred within the threaded region.

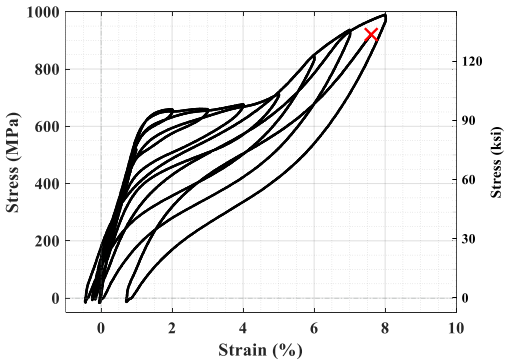

(a)

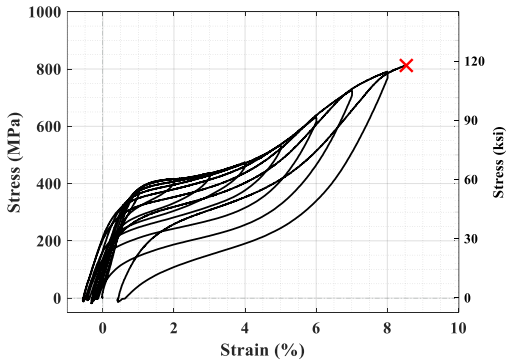

(b)

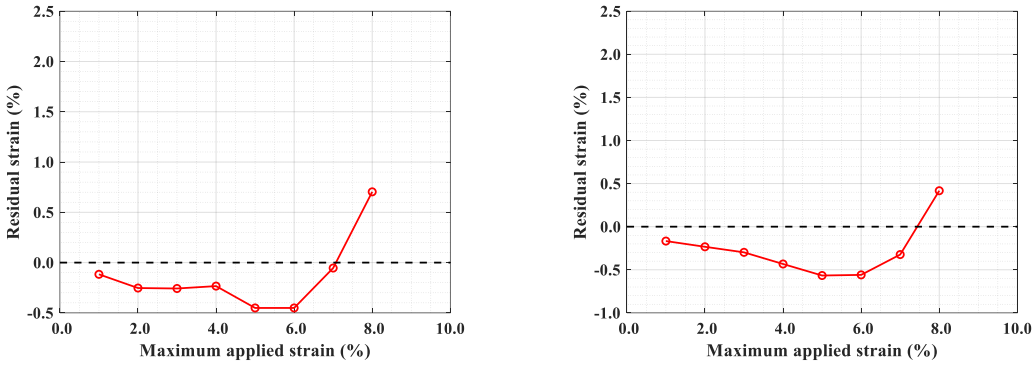

(c) (d)

Figure 3-3 Result of 1% strain cyclic loading until failure at 23 ℃: (a) Ni-Ti-Co stress-strain curve, (b) Ni-Ti stress-strain curve, (c) Ni-Ti-Co residual strain , and (d) Ni-Ti residual strain.

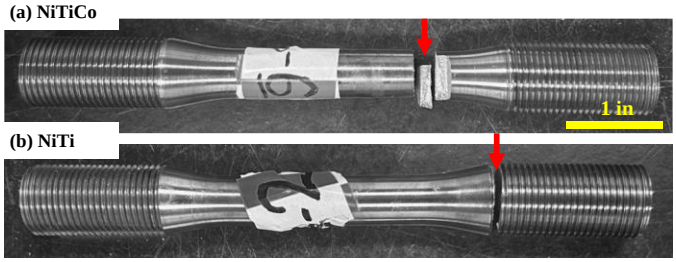

Figure 3-4 Photos of fractured (a) Ni-Ti-Co, and (b) Ni-Ti samples after 1% strain incremental cyclic loading until failure at 23 ℃.

The residual strain, ε_{resi}, versus maximum strain, ε_{max}, of Ni-Ti-Co and Ni-Ti are shown in Figure 3-3 (c) and (d), respectively. It is seen that when the strain is smaller than 7%, both Ni-Ti-Co and Ni-Ti SMA exhibit negative residual strain. The negative residual strain indicates the sample shortened during unloading, which may be caused by the release of residual stress generated when manufacturing or heat-treating the alloy. More research is needed to further understand this phenomenon. Overall, ε_{resi} in Ni-Ti-Co SMA was close to that of the Ni-Ti SMA. When the applied strain reached 8%, ε_{resi}, of Ni-Ti-Co SMA was only 0.7%, indicating the excellent strain recovery of Ni-Ti-Co SMA.

The strain recovery capacity of Cu-Al-Mn SMA has been investigated by the authors in a previous study (Hong et al. 2022a). The σ_y of Cu-Al-Mn SMA was 274 MPa (39.7 ksi) and the fracture strain was 11.7%. Assuming that a residual strain of 0.25% or less indicates full superelastic behavior, the maximum strain at which Cu-Al-Mn SMA was superelastic was 7.6%. This limit for Ni-Ti-Co and NiTi was approximately 7%. The yield stress of Ni-Ti-Co SMA was approximately 1.6 times that of Ni-Ti SMA and 2.3 times that of Cu-Al-Mn SMA.

b) Temperature dependence

Stress-strain curves of Ni-Ti-Co, Ni-Ti and Cu-Al-Mn SMA at different temperatures are shown in Figure 3-5. It is noted that all the results in Figure 3-5 (a) were obtained using the same Ni-Ti-Co sample and the results in Figure 3-5 (b) were obtained using the same Ni-Ti sample. In other words, after testing at one target temperature, the sample was tested again at the other temperatures. In Figure 3-5 (c), since it is known that the superelastic behavior of Cu-Al-Mn SMA is sensitive to the crystal orientation (Kise et al. 2021; Omori et al. 2020). To eliminate the influence of crystal orientation and obtain a better understanding of the effect of temperature, results in Figure 3-5 (c) were measured from Cu-Al-Mn samples with the same crystal structure. During the tests on Ni-Ti-Co SMA at 50 °C and Ni-Ti SMA at -20 °C, the incremental cyclic loading was terminated (as marked by the circle) when some residual strain was observed after unloading. After the termination, the sample was unloaded to zero force and tested again at other temperatures.

From Figure 3-5, it is seen that Ni-Ti-Co SMA shows flag-shape stress-strain curves at 23°C, 0°C, -20°C and -40°C. There was almost no residual strain up to a cyclic loading amplitude of 5%, indicating excellent strain recovery. When the temperature was 50°C, the

residual strain started to accumulate at around 3% cyclic strain amplitude. After unloading from 4%, the residual strain was over 0.5%. Compared with Ni-Ti and Cu-Al-Mn SMA shown in Figure 3-5 (b) and (c), it is seen that the temperature range at which Ni-Ti-Co SMA maintains superelasticity is wider than that of Ni-Ti SMA (which loses strain recovery at -20 °C) and comparable to that of Cu-Al-Mn SMA.

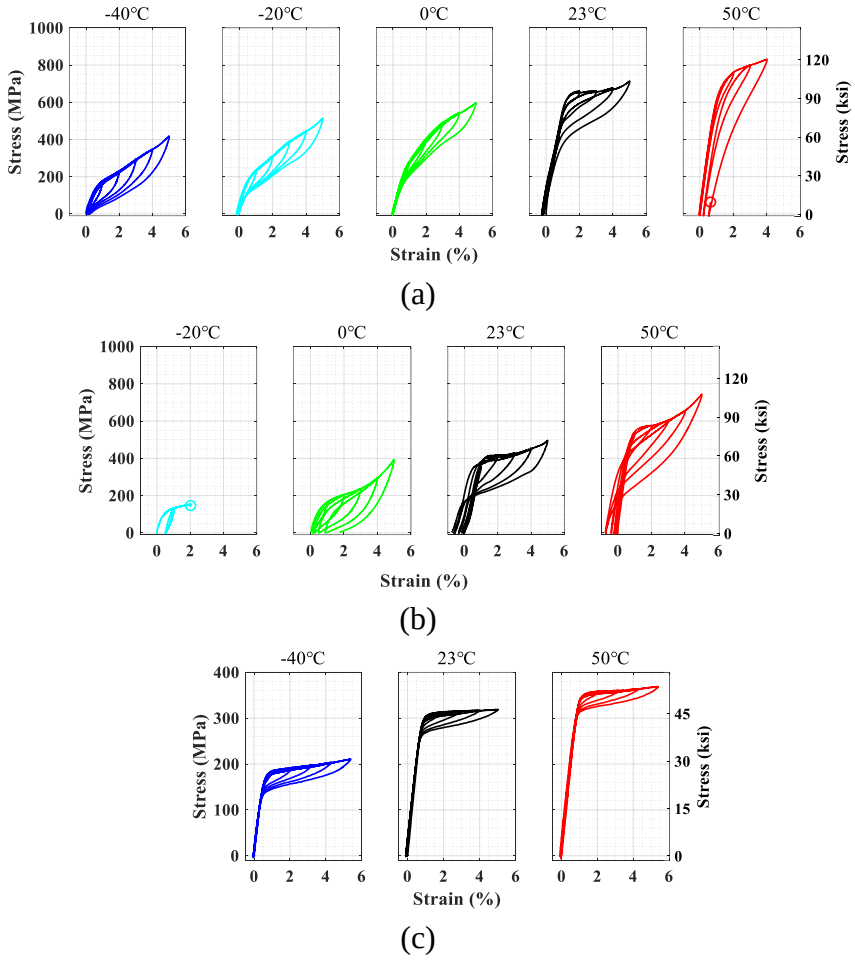

Figure 3-5 Stress-strain curves at different temperatures: (a) Ni-Ti-Co, (b) Ni-Ti, and (c) Cu-Al-Mn SMA.

3.3.2 Low-cycle fatigue tests

a) Room temperature behavior

The low-cycle fatigue stress-strain curves of Ni-Ti-Co SMA at 23 ℃ are shown in Figure 3-6 (a). The material exhibited a clear flag-shape stress-strain curve during the first cycle, however, the width of hysteresis loops and the yield strength degraded rapidly within five cycles. From fifth to 10th cycles, the yield strength showed a continuous decrease and the width of the hysteresis loop narrowed gradually. After 10th cycles, the stress-strain curves of Ni-Ti-Co SMA stabilized until fracture at 92 cycles. It is noted that, even though the yield strength and the width of hysteresis loop of Ni-Ti-Co SMA showed a rapid reduction and fractured within 100 cycles, its strain recovery capacity was maintained up to failure Almost no residual strain accumulation was observed during the low-cycle fatigue loading of Ni-Ti-Co SMA at 23°C. A photo of fractured sample is shown in Figure 3-6 (b). Similar to the result shown in Figure 3-4 (a), the Ni-Ti-Co SMA fractured into three pieces, see Figure 3-6 (b), both of the fractures occurred within the threaded regions.

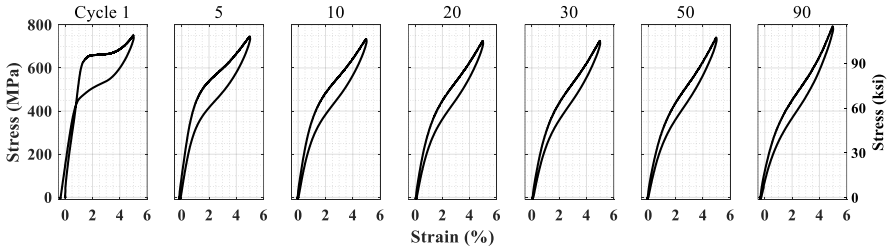

(a)

(b)

Figure 3-6 Low-cycle fatigue results of Ni-Ti-Co SMA at 23°C: (a) stress-strain curves, and (b) fractured sample.

The low-cycle fatigue stress-strain curves of Ni-Ti SMA at 23 °C are shown in Figure 3-7 (a). Ni-Ti SMA showed a similar trend of degradation in superelasticity during fatigue loading with Ni-Ti-Co SMA. The difference was that the yield strength and the width of the hysteresis loops of Ni-Ti SMA decreased slower than that of Ni-Ti-Co SMA. Up to 10 cycles, the yield stress in Ni-Ti SMA reduced slightly and stabilized at around 20 cycles. The fatigue life of Ni-Ti SMA was close to but slightly higher than that of Ni-Ti-Co SMA. The NiTi SMA fractured at 104 cycles. It is worth noting that as the number of cycles increased, the maximum stress of Ni-Ti SMA at 5% showed a remarkable increase. This phenomenon may be caused by the strain hardening of Ni-Ti SMA that did not occur in Ni-Ti-Co SMA. A photo of fractured sample is shown in Figure 3-7 (b). The failure occurred in the threaded end.

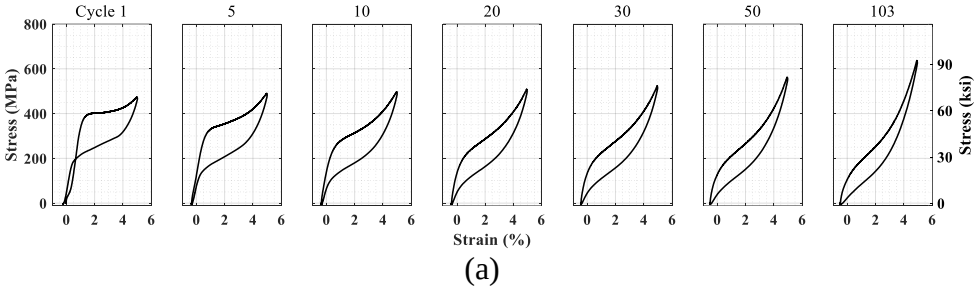

(a)

(b)

Figure 3-7 Low-cycle fatigue results of Ni-Ti SMA at 23°C: (a) stress-strain curves, and (b) fractured sample.

The extracted parameters of Ni-Ti-Co and Ni-Ti SMA with respect to loading cycles at 23°C are shown in Figure 3-8. Comparing the extracted parameters of Ni-Ti-Co and Ni-Ti SMA, it is seen that Ni-Ti-Co SMA shows an overall higher degradation rate than Ni-Ti SMA. Take cycle 10 as an example, the Young's modulus, E_{load}, yield stress, σ_y, and damping ratio, δ_R of Ni-Ti-Co SMA were respectively around 75%, 69% and 62% of the initial values; while in Ni-Ti SMA, the E_{load} showed almost no decrease, and the σ_y and δ_R were

respectively 80% and 89% of the initial cycle. In the last cycle, the σ_y, and δ_R of Ni-Ti-Co SMA were respectively 53% and 52% of the initial cycle. While for Ni-Ti SMA, the σ_y, and δ_R were 36% and 64% of the initial cycle. The residual strain, ε_{resi}, of both Ni-Ti-Co and Ni-Ti SMA remained near-zero throughout the low-cycle fatigue loading. It is noted that the Ni-Ti SMA showed a higher negative strain during fatigue loading, which led to a slight increase of the recovery strain ε_{reco}. In the last cycle, the ε_{resi} and ε_{reco} of Ni-Ti-Co SMA were -0.24% and 5.2%, respectively; while the ε_{resi} and ε_{reco} of Ni-Ti SMA were -0.56% and 5.5%, respectively.

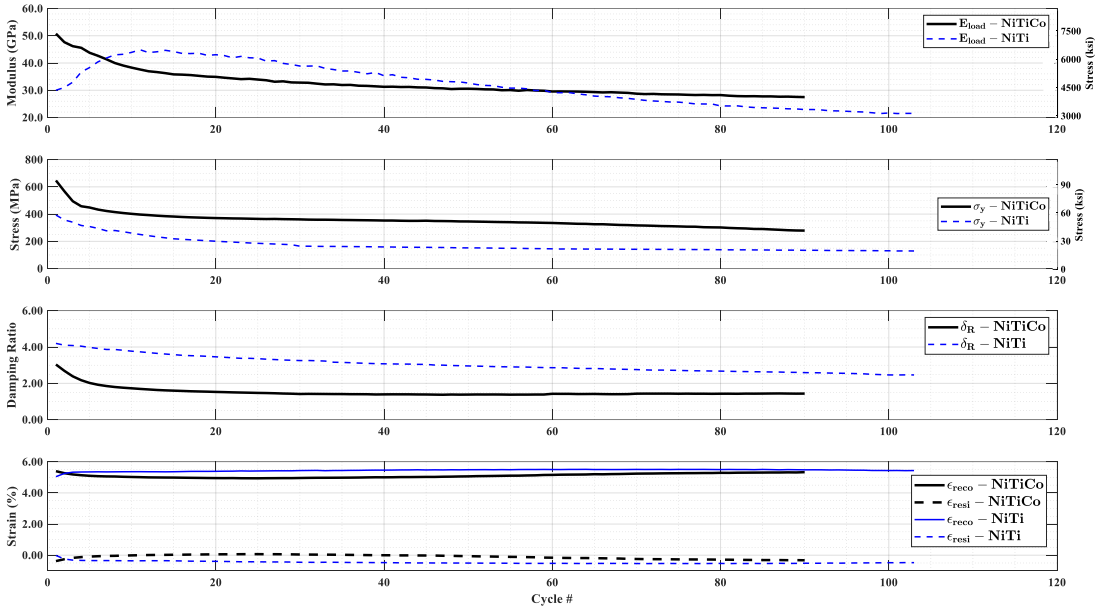

Figure 3-8 Variation in mechanical properties of Ni-Ti-Co and Ni-Ti SMA at 23 °C.

b) Low temperature behavior

The low-cycle fatigue stress-strain curves of Ni-Ti-Co SMA at -40°C are shown in Figure 3-9 (a). Compared with the results at 23°C, it is seen that Ni-Ti-Co SMA showed a much wider hysteresis loop width at -40°C. Furthermore, it is worth noting that the stress-strain curves have a minor degradation up to 100 cycles (although the yield stress decreased slightly,

the narrowing of the hysteresis loop was negligible). From 150 to 471 cycles, when fracture occurred, the hysteresis loop widths narrowed down slightly and the residual strain accumulated gradually. The fractured sample is shown in Figure 3-9 (b), where the sample broke at the thread end. Overall, compared with room temperature behavior, Ni-Ti-Co SMA showed improved low-cycle fatigue performance in terms of both fatigue life and stress-strain hysteresis curves at -40 °C.

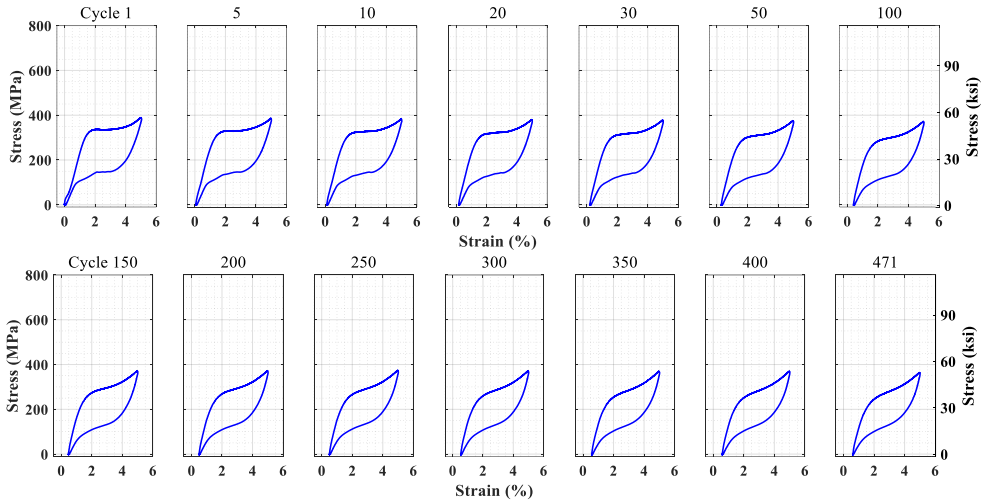

(a)

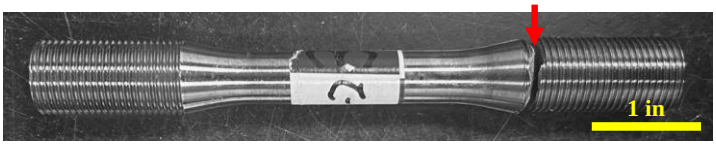

(b)

Figure 3-9 Low-cycle fatigue results of Ni-Ti-Co SMA at -40°C: (a) stress-strain curves, and (b) fractured sample.

The low-cycle fatigue stress-strain curves of Ni-Ti SMA samples at 0°C are shown in Figure 3-10. Different from the Ni-Ti-Co SMA shown in Figure 3-9, the hysteresis loops of Ni-Ti SMA showed significant narrowing and the yield stress of Ni-Ti SMA decreased more significantly in the first 100 cycles. From 100 to 800 cycles, at which the test was terminated, the Ni-Ti SMA response was stabilized, and the shape of hysteresis loop exhibited little degradation. The sample was still intact because the fatigue loading was terminated at 800

cycles when a stabilized stress-strain response was observed. Therefore, no photo of fractured sample is presented.

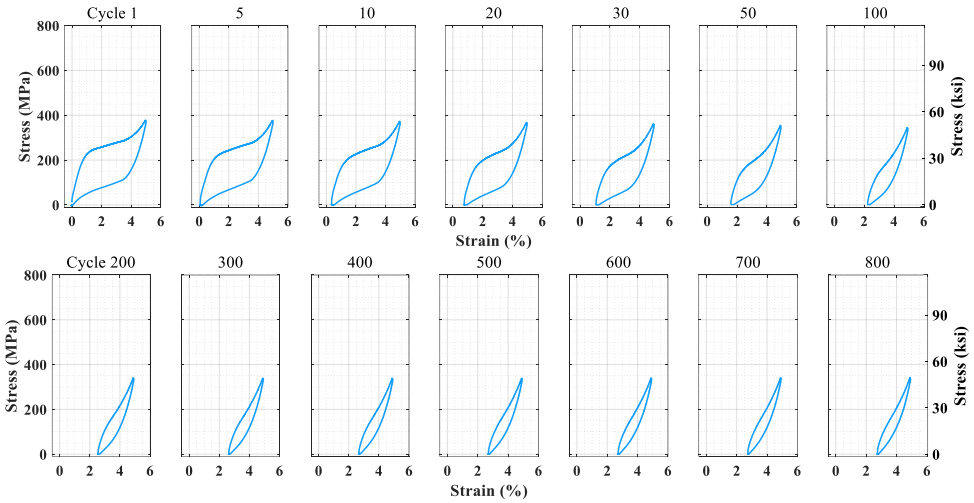

Figure 3-10 Low-cycle fatigue stress-strain curves of Ni-Ti SMA at 0°C.

The extracted parameters of Ni-Ti-Co at -40 °C and Ni-Ti SMA at 0 °C with respect to loading cycles shown in Figure 3-11. It is seen that the superelasticity degradation of Ni-Ti-Co SMA at 40 °C was slower with increasing cycles than that of Ni-Ti SMA at 0 °C. For example, at 100 cycles, the Young's modulus, E_{load}, yield stress, σ_y, and damping ratio, δ_R of Ni-Ti-Co SMA were respectively 94%, 83% and 90% of those during the first cycle; the recovery strain ε_{reco} of Ni-Ti-Co SMA showed almost no decrease. While for Ni-Ti SMA, E_{load}, σ_y, and δ_R at 100 cycles were respectively 77%, 51% and 36% of those during the first cycle; ε_{resi} up to 2.3% was observed; and ε_{reco} of Ni-Ti SMA at 100 cycles was 53% of that at the first cycle. In the last cycle, E_{load}, σ_y, and δ_R of Ni-Ti-Co SMA were respectively 78%, 70% and 77% of those during the first cycle; while for Ni-Ti SMA, E_{load}, σ_y, and δ_R were respectively 75%, 39% and 23% of those during the first cycle. The ε_{reco} of Ni-Ti-Co SMA decreased by 12% when it fractured while the same value for Ni-Ti SMA was 45%.

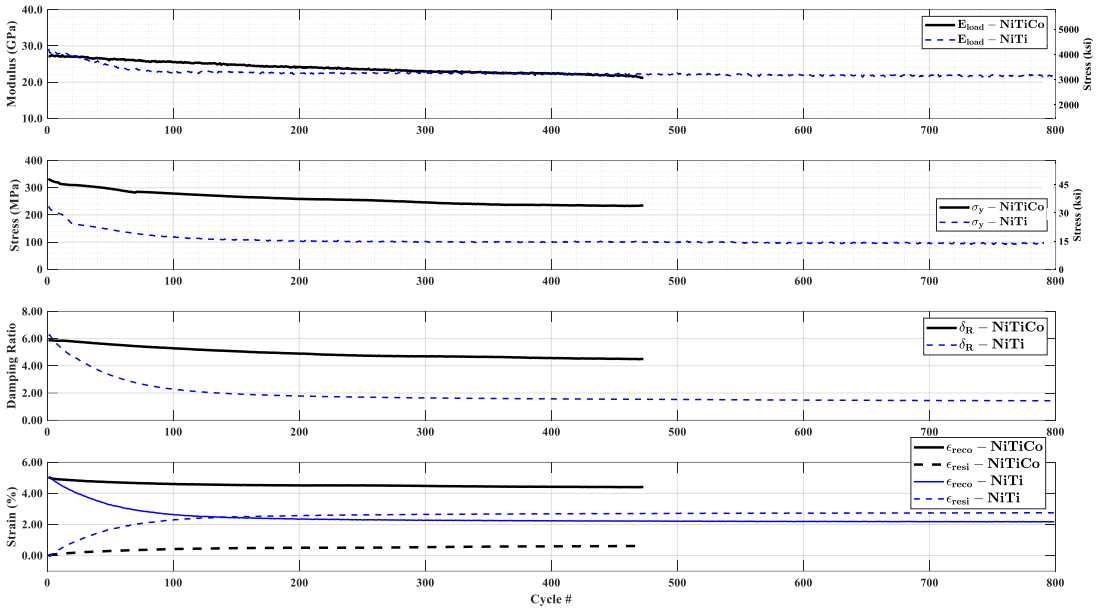

Figure 3-11 Variation in mechanical properties of Ni-Ti-Co at -40°C and Ni-Ti SMA at 0°C.

c) High temperature, 50 ℃

The low-cycle fatigue stress-strain curves of Ni-Ti-Co SMA at 50°C are shown in Figure 3-12 (a). The stress-strain curve of Ni-Ti-Co SMA is not ideally flag-shaped even in the first cycle because the austenitic transformation finish point disappeared during unloading and a residual strain of approximately 0.8% was observed. Up to fifth cycle, large reduction in the area of hysteresis curves was observed, and the martensitic transformation start point also disappeared. From fifth to 48th cycle, at which the bar fractured the hysteresis loop showed almost no change indicating the Ni-Ti-Co SMA was stabilized after five cycles of fatigue loading. The fractured sample is shown in Figure 3-12 (b), where the sample broke at the thread end. Compared with the results at 23°C and -40°C, Ni-Ti-Co SMA showed faster stabilization, more significant hysteresis pinching, and a larger residual strain accumulation at 50°C.

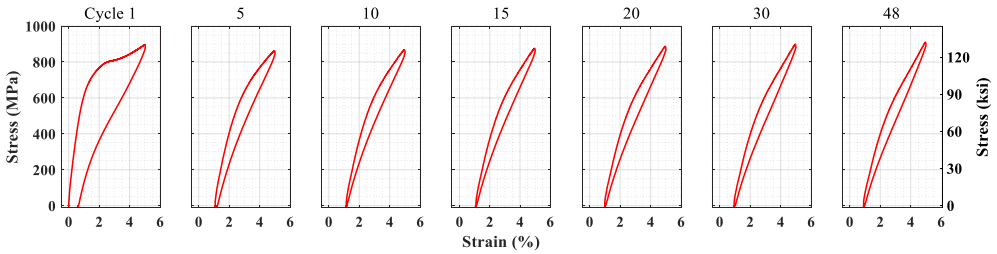

(a)

(b)

Figure 3-12 Low-cycle fatigue results of Ni-Ti-Co SMA at 50°C: (a) stress-strain curves, and (b) fractured sample.

The low-cycle fatigue stress-strain curves of Ni-Ti SMA samples at 50 °C are shown in Figure 3-13 (a). Similar to Ni-Ti-Co SMA, the Ni-Ti SMA exhibited rapid stabilization and reduction in the area of the hysteresis curves within the first five cycles. From the fifth up until the 71st cycle, at which fracture occurred, the hysteresis loop width narrowed gradually. The difference from Ni-Ti-Co SMA was that Ni-Ti SMA had less residual strain accumulation, and the maximum stress at 5% strain showed a more significant increase compared to the first cycle. The fractured sample is shown in Figure 3-13 (b), where the failure occurred within the gauge length. No obvious necking was observed.

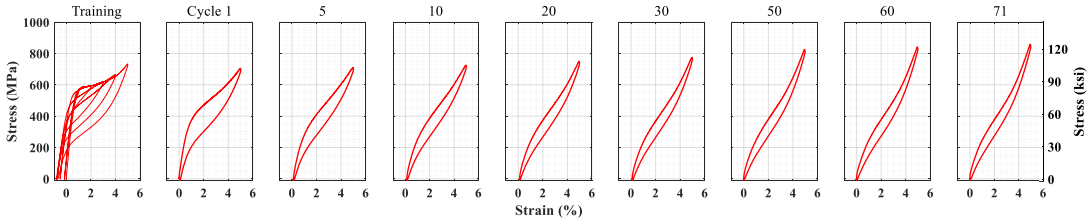

(a)

(b)

Figure 3-13 Low-cycle fatigue results of Ni-Ti SMA at 50°C: (a) stress-strain curves, and (b) fractured sample.

The extracted parameters of Ni-Ti-Co and Ni-Ti SMA with respect to loading cycles at -50°C are shown in Figure 3-14. The Ni-Ti-Co SMA overall had more significant superelasticity degradation (in terms of energy dissipation and strain recovery) than Ni-Ti SMA. Take the 10th cycle for example, E_{load}, σ_y, δ_R and ε_{reco} of Ni-Ti-Co SMA were respectively 54%, 78%, 31% and 87% of those during the first cycle; while E_{load}, σ_y, δ_R and ε_{reco} of Ni-Ti-Co SMA were respectively 53%, 72%, 67% and 97% of those during the first cycle. In the last cycle, E_{load}, σ_y, and δ_R of Ni-Ti-Co SMA were respectively 47%, 69% and 29% of those during the first cycle, whereas those values for Ni-Ti SMA were 41%, 62% and 53%, respectively. The recovery strain, ε_{reco}, of Ni-Ti SMA decreased by 8% when it fractured while the value for Ni-Ti SMA was less than 1%.

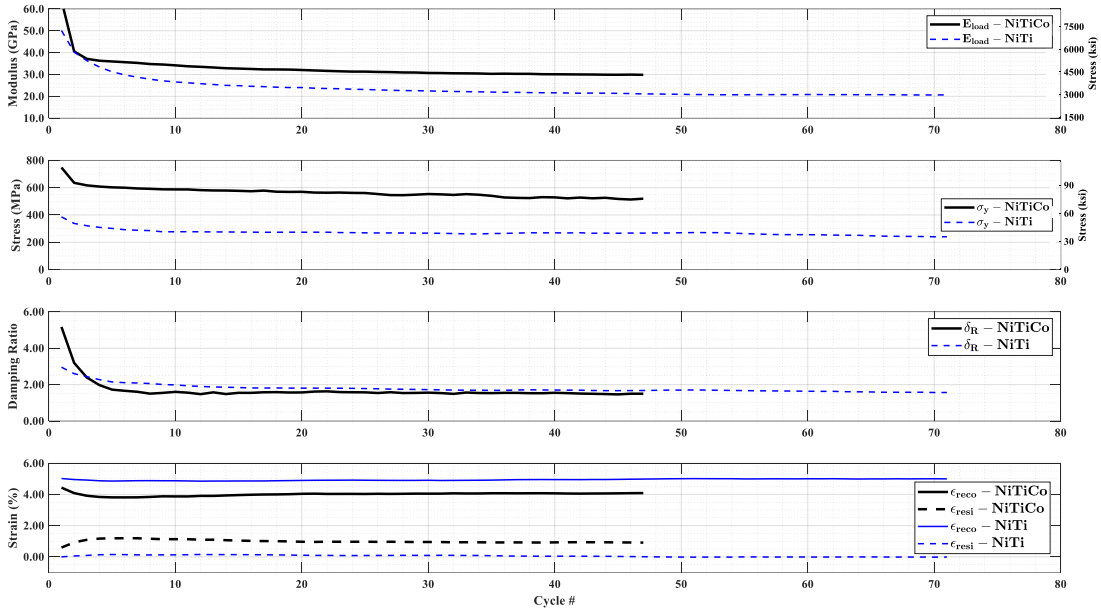

Figure 3-14 Variation in mechanical properties of Ni-Ti SMA at 50°C.

3.4 Summary

At room temperature 23°C, Ni-Ti-Co SMA exhibited excellent superelastic behavior in terms of its flag-shaped stress-strain curves and strain recovery capacity. The maximum recovery strain of Ni-Ti-Co SMA (around 7%) was close to that of Ni-Ti SMA and smaller

than that of Cu-Al-Mn SMA (around 7.6%). The fracture strain of Ni-Ti-Co SMA (around 8%) was lower than that of Ni-Ti SMA (8.5%) and that of Cu-Al-Mn SMA (12.7%). Ni-Ti-Co SMA exhibited ideal flag-shape stress-strain curves at 23℃, 0℃, -20℃ and -40℃. There was almost no residual strain when the cyclic strain loading was 5%, indicating excellent strain recovery capacity and wide application temperatures. Compared with Ni-Ti SMA and Cu-Al-Mn SMA: Ni-Ti SMA lost superelasticity when temperature dropped to 0 ℃, and Cu-Al-Mn SMA showed stable superelasticity from -40 ℃ to 50 ℃. Therefore, it was concluded that the temperature range of Ni-Ti-Co SMA is close to that of Cu-Al-Mn SMA and wider than that of Ni-Ti SMA. It is noted that the superelasticity of Ni-Ti-Co SMA decreased at 50℃. Specifically, the residual strain started to accumulate at around 3% cyclic strain amplitude; after unloading from 4%, the residual strain was around 0.5%.

Regarding the low-cycle fatigue resistance, at 23 ℃, the low-cycle fatigue resistance of Ni-Ti-Co SMA was similar to that of Ni-Ti SMA in terms of fatigue life and superelasticity degradation. Both materials fractured after about 100 cycles of 5% constant strain fatigue loading, and neither material had appreciable residual strain accumulation before fracture meaning that the strain recovery capacity throughout the fatigue loading was stable. It is noted that the yield strength and energy dissipation capacity of Ni-Ti-Co SMA decreased faster than those of Ni-Ti SMA.

Ni-Ti-Co SMA showed excellent fatigue resistance when temperature was reduced to -40℃. Compared to Ni-Ti SMA at 0℃, the yield strength, energy dissipation and strain recovery of Ni-Ti-Co SMA showed much lower degradations. There was no loss of yield strength, energy dissipation, and strain recovery of Ni-Ti-Co SMA during the first 100 cycles of fatigue loading. From 100 to 471 cycles (when fracture occurred), the strain recovery

showed almost no degradation. These characteristics indicate the potential of applying Ni-Ti-Co SMA in bridges subjected to low temperatures.

At 50°C, the low-cycle fatigue resistance of Ni-Ti-Co SMA was lower than that at 23 °C and lower than that of Ni-Ti SMA at 50°C. The hysteresis loops of Ni-Ti-Co at 50°C narrowed quickly (within five cycles), leading to a disappearance of the martensitic transformation start and austenitic transformation finish points, as well as a significant decrease in the energy dissipation capacity. It is noted that the strain recovery of Ni-Ti-Co at 50°C had no degradation during the fatigue loading.

It is worth noting that most of the Ni-Ti-Co and Ni-Ti SMA samples tested in this study fractured at the threaded ends due to stress concentration. That means the true fracture strain and low-cycle fatigue life of these two materials are larger than the reported values. Since the main purpose of this study was to characterize the superelasticity degradation of Ni-Ti-Co SMA under varying temperatures and seismic loads, more attention was paid to the superelastic properties variations rather than the fatigue lives. To further understand this issue, more research on samples with reduced gauge length diameters, or studies targeted on the fracture toughness of Ni-Ti-Co SMA are needed.

CHAPTER 4 MOMENT-CURVATURE ANALYSIS OF TYPICAL BRIDGE COLUMNS

4.1 Introduction

In Chapter 3, it is seen that Ni-Ti-Co SMA shows a higher yield strength than that of Ni-Ti SMA (1.6 times) and Cu-Al-Mn SMA (2.3 times). Large diameter bars with diameters of 30 mm (1.2 in) or more for all the three types have been made available in the past. Both the high strength and availability in large diameters of Ni-Ti-Co SMA make it potentially suitable for real bridge applications. However, no research has been performed on structural properties of bridge columns reinforced with Ni-Ti-Co SMA.

Moment-curvature analyses using Open System for Earthquake Engineering Simulation (OpenSees) PEER (2000) were performed to investigate the flexural behavior of Ni-Ti-Co SMA reinforced sections for possible implementation in typical bridge columns. For comparison purposes, columns reinforced with Ni-Ti and Cu-Al-Mn SMA bars were also investigated. Conventional reinforced concrete (RC) bridge column sections were also analyzed as benchmarks to determine the reference plastic moments. The influence of key parameters: column section diameter, longitudinal reinforcement ratio and axial force ratio were investigated.

FeSMA was not considered here because columns reinforced with FeSMA are inherently different from columns reinforced with Ni-Ti-Co, Ni-Ti, and Cu-Al-Mn SMAs. Columns reinforced with Ni-Ti-Co, Ni-Ti and Cu-Al-Mn SMAs primarily exploit the superelastic property of SMA bars to eliminate permanent drifts. The control parameters of columns reinforced with Ni-Ti-Co, Ni-Ti and Cu-Al-Mn SMAs are the same as those of conventional RC columns, such as reinforcement ratio and axial force ratio. Whereas

columns reinforced with FeSMA are more closely related to rocking columns. The control parameters include the prestrain level of FeSMA bars, and the initial prestress level on the column. Furthermore, the constitutive model of FeSMA bars for use in rocking columns remains to be developed. Considering the difference between FeSMA reinforced columns and columns reinforced with superelastic SMAs, as well as the limitation in constitutive model of FeSMA, only Ni-Ti and Cu-Al-Mn SMAs were selected to make comparison with Ni-Ti-Co SMA reinforced columns.

4.2 Modeling method

4.2.1 RC columns

Moment-curvature analysis using OpenSees was performed on RC and SMA columns. The analysis of RC column sections includes three components, namely, unconfined concrete cover, longitudinal bars, and confined concrete core. The effect of the transverse reinforcement was accounted for in the confined concrete properties. Concrete01 material was used to model the unconfined concrete cover and Concrete04 material was used to model the confined concrete core. Mander's model (Mander et al. 1988) was used to determine the properties of both unconfined and confined concrete. The tensile strength of concrete was ignored in all analyses. ReinforcingSteel material was used to model the longitudinal steel bars. Constitutive models used in RC columns are shown in Figure 4-1.

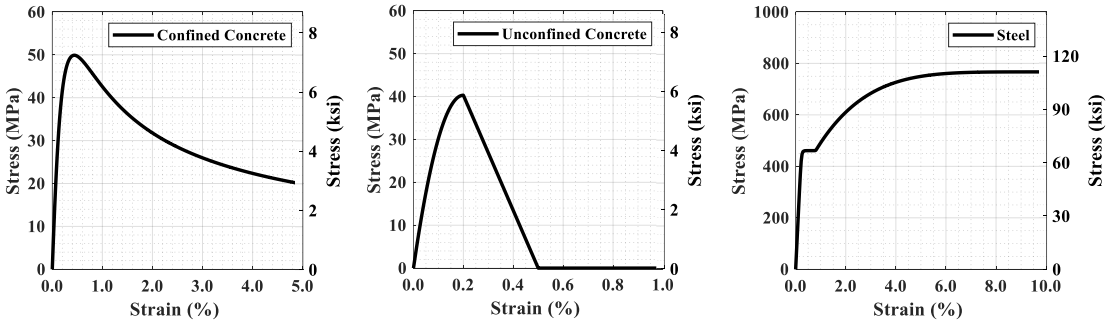

(a) (b) (c)

Figure 4-1 Constitutive models used in RC columns: (a) confined concrete, (b) unconfined concrete, and (c) steel rebar.

A full-scale RC bridge column (Schoettler et al. 2015) with a section diameter D = 1.22 m (4 ft) was used as the reference column to validate the OpenSees model. This column model represents the typical single-column bridge bents commonly used in California and is designed according to the Caltrans Bridge Design Specifications and Seismic Design Criteria. The cross section of the reference column is shown in Figure 4-2 (a). Grade 60 steel was used with a longitudinal reinforcement ratio of 1.55% and transverse reinforcement ratio of 0.95%. The axial load was 2530 kN (575 kip), with an axial force ratio of a = 5.3%. Normal weight concrete with a compressive strength of 40.3 MPa (5.8 ksi).was used in the entire column. Additional information can be found in Schoettler et al. (2015). The simulated result is compared with the idealized test result in Figure 4-2 (b). It is seen that the results from the OpenSees model matches well with the idealized test result.

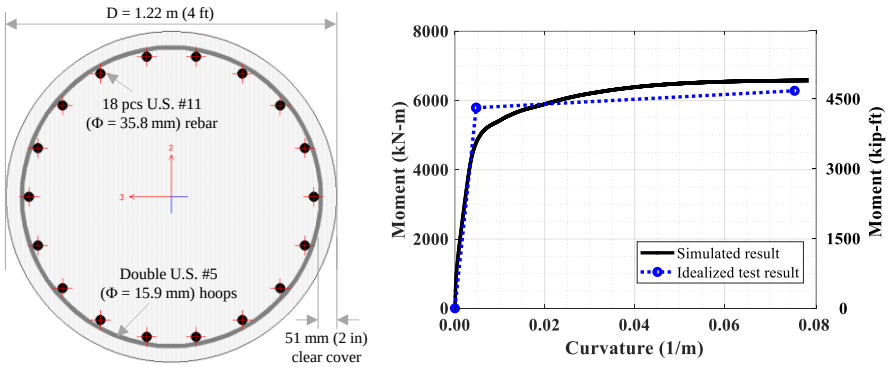

(a) (b)

Figure 4-2 (a) Section details of reference column, and (b) validation of established OpenSees model.

4.2.2 SMA reinforced columns

Engineered cementitious composite (ECC) is a fiber reinforced mortar often used in the plastic hinge regions to reduce and delay plastic hinge damage such as that due to concrete spalling. Compared with conventional concrete, ECC has a high tensile strength and ductility. Multiple cracks with a width of less than 100 μm form under tensile loading giving the ECC ability to deform significantly before failure. The advantages of ECC complement the strain recovery of SMA, and the combination of the two could help keep bridge columns in service even after strong earthquakes. The moment curvature analyses conducted in this study used this combination when the longitudinal steel reinforcement was replaced with SMA. The transverse reinforcement was assumed to be mild steel in the SMA columns.

The SMA column section includes three components, namely unconfined ECC cover, longitudinal SMA bars, and confined ECC core. Similar to the RC columns, the effect of transverse reinforcement is implicit in the confined ECC properties. Both the unconfined ECC cover and confined ECC core were modeled by Concrete02 material, using constitutive models developed by Motaref (2011b). To be consistent with the modeling methods used in the RC column, the tensile strength of ECC was also ignored. SelfCentering material was used to model the SMA bars, i.e., Ni-Ti-Co, Ni-Ti and Cu-Al-Mn SMA. For brevity, they are referred to as NiTiCo, NiTi and CAM SMA, respectively, hereafter. The key parameters in SelfCentering material are shown in Figure 4-3, blue solid line. SMA bars were connected to the steel rebar that were embedded in the footing and cap beam. The bond slip of the steel rebar was accounted for using the method developed by Tazarv et al. (2014). The modified stress-strain curves of SMA are shown in Figure 4-3

in green dashed lines. The parameter used to model NiTiCo, NiTi and CAM SMA bars are listed in Table 4-1.

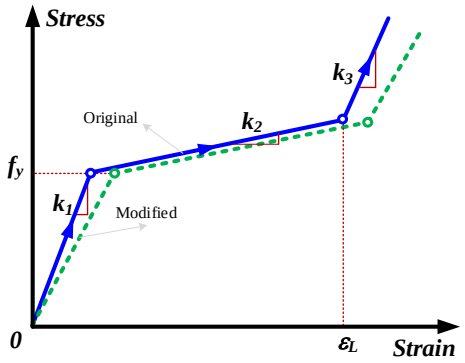

Figure 4-3 Definition of key parameter used to model SMA bars.

Table 4-1 Details of properties used to model SMA bars.

Properties			NiTiCo	NiTi	CAM
Yield stress	f_y	(MPa)	631	396	273
		(ksi)	91.5	57.4	39.6
Martensitic finish strain	ε_L	(%)	4.9	4.5	6.2
Austenite modulus	k_1	Original (GPa)	40	35	65
		Original (ksi)	5802	5076	9427
		Modified (GPa)	24.2	22.2	46.2
		Modified (ksi)	3510	3220	6701
Post-yield stiffness	k_2	Original (GPa)	1	2.3	1.4
		Original (ksi)	145	334	203
		Modified (GPa)	2	2.2	1.4
		Modified (ksi)	290	319	203
Post-hardening stiffness	k_3	Original (GPa)	9.3	9.1	34.1
		Original (ksi)	1349	1320	4946
		Modified (GPa)	8.1	7.9	30.1
		Modified (ksi)	1175	1146	4366

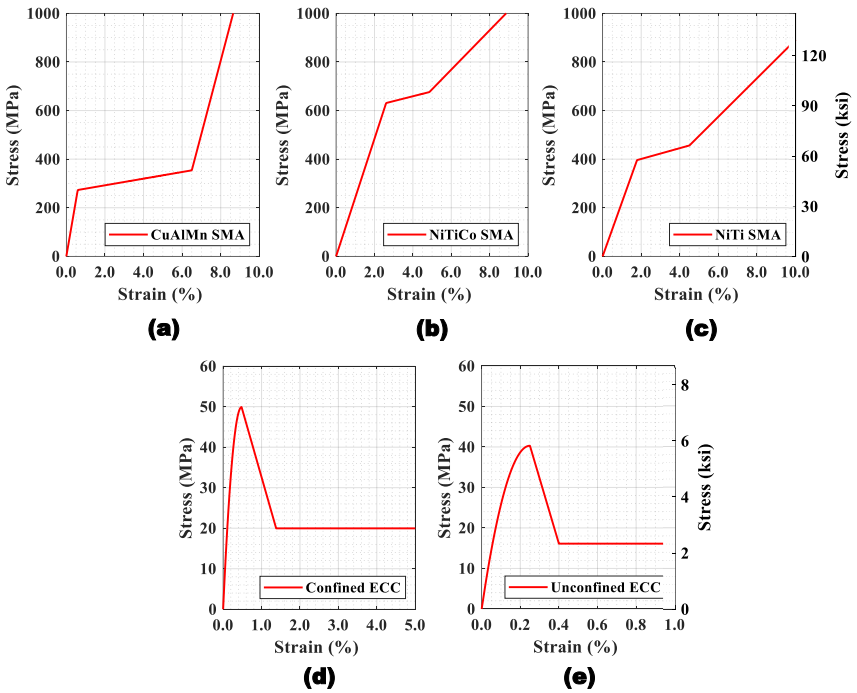

Figure 4-4 Stress-strain curves used to model SMA columns: (a) CAM SMA, (b) NiTiCo SMA, (c) NiTi SMA, (d) confined ECC, and (e) unconfined ECC.

4.3 Methodology

The criterion to design SMA reinforced column section details was to match the plastic moment with their corresponding reference RC column sections. It is realized that matching the plastic moment ignores the fact that the relatively low SMA reinforced column stiffness could affect the plastic moment demand in the bridge columns. Typical moment-curvature (M-Phi) diagrams of RC and SMA columns are shown in Figure 4-5. For the RC column shown in Figure 4-5 (a), the actual M-Phi curve (O-A-B) can be idealized with an elasto-plastic response (O-C-E) according to AASHTO LRFD Bridge Design Specifications (AASHTO 2011). Point A in Figure 4-5 (a) is at the first longitudinal reinforcing bar yielding, and the idealized plastic moment at point C, M_p, is obtained by equating the area between the actual and the idealized response beyond point A, i.e., the blue shaded region (ACD) and the red shaded region (BDE). The ultimate curvature, ϕ_u, is

determined when the compressive strain of concrete reaches 0.018, which is 1.5 times the value in Mander et al. (1988) because as reported by Motaref et al. (2011b), the ultimate strain of concrete measured from the column tests is significantly higher than the value computed by the Mander's model (Mander et al. 1988).

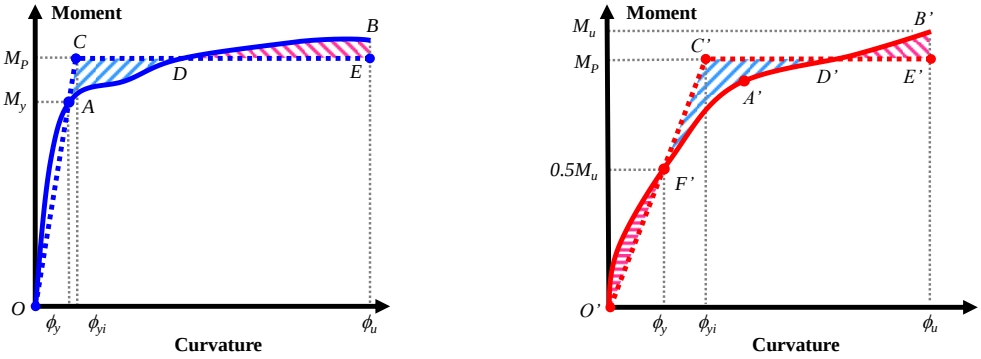

(a) (b)

Figure 4-5 Typical moment-curvature curves of: (a) RC column, and (b) SMA column.

The shape of the moment-curvature relationship for SMA reinforced column sections is generally very different than that of RC section as seen in Figure 4-5 (b). Therefore, the idealization method in LRFD Bridge Design Specifications (AASHTO 2011) was modified as follows. First, the ultimate curvature, ϕ_u, is reached when the compressive strain at the edge of the ECC core reaches 0.03, which is 1.5 times of the value computed using the method in Motaref at al. (2011b). Second, the elastic portion of the idealized curve passes through the $0.5M_u$, i.e., point F' in Figure 4-5 (b). The same approach was also adopted by Pulido et al. (2004) for concrete sections with properties significantly different than that of RC. Third, to obtain the idealized plastic moment at point C', M_p, the red shaded region in O'F' plus B'D'E' was added up to equate the blue shaded region C'D'F'.

Using the above methods, the idealized plastic moment of RC column and SMA column was obtained and compared for a range of parameters. Nine conditions were considered for RC columns, including three section diameters (D = 4, 5 and 6 ft), three reinforcement ratios (r = 1%, 2% and 3%) and three axial force ratios (a = 5%, 10% and 15%). The control RC column had D = 5 ft, r = 2%, a = 10%. The steel rebar was 35.8 mm (1.41 in) diameter (U.S. #11), with a yield strength of 461MPs (67 ksi). Conventional concrete was used with a compressive strength of 40.3 MPa (5.8 ksi). The clear cover was 51 mm (2 in). The test matrix of moment-curvature analyses is shown in Figure 4-6. One parameter was changed at a time in the moment curvature analysis. It is noted that only a circular column section was considered in this study.

		Section diameter ***D*** (ft)	Reinforcement ratio ***r*** (%)	Axial froce ratio ***a*** (%)
RC	RC-1	4	2	10
	RC-2	5		
	RC-3	6		
	RC-4	5	1	10
	RC-5		2	
	RC-6		3	
	RC-7	5	2	5
	RC-8			10
	RC-9			15

NiTiCo	**NiTi**	**CAM**
NiTiCo-1.x	NiTi-1.x	CAM-1.x
NiTiCo-2.x	NiTi-2.x	CAM-2.x
NiTiCo-3.x	NiTi-3.x	CAM-3.x
NiTiCo-4.x	NiTi-4.x	CAM-4.x
NiTiCo-5.x	NiTi-5.x	CAM-5.x
NiTiCo-6.x	NiTi-6.x	CAM-6.x
NiTiCo-7.x	NiTi-7.x	CAM-7.x
NiTiCo-8.x	NiTi-8.x	CAM-8.x
NiTiCo-9.x	NiTi-9.x	CAM-9.x

Note: The section diameter or number of longitudinal bars of NiTiCo, NiTi and CuAlMn SMA section is iterated until its plastic moment matches the corresponding RC column. '**-.x**' means no. x of iteration.

Figure 4-6 Test matrix of moment-curvature analyses.

Three types of SMA reinforced columns were analyzed, namely NiTiCo, NiTi and CAM SMA. The largest diameters of SMA bars used in past studies were assumed: 32 mm (1.26 in) NiTiCo, 27 mm (1.06 in) NiTi, and 30 mm (1.18 in) CAM SMA bars. Concrete cover of all SMA reinforced columns was the same as that of RC columns, but the number

of longitudinal bars or the section diameter was adjusted to match M_p of the corresponding RC sections.

Matching of M_p required consideration of the differences between the SMA and RC sections. From Figure 4-5, it is seen that the SMA column has a different M-Phi response than the RC column. Because the yield strength and Young's modulus of SMA bars are different than those of steel bars, the number of SMAs bars was adjusted so that the SMA and RC section M_p values are the same. However, there is an upper limit on the number of longitudinal bars due to the required minimum spacing (AASHTO 2011).

An iterative process was used to design the RC-equivalent SMA reinforced sections. The number of SMA bars was increased first, when the clear spacing between the longitudinal bars reached the upper limit and the moment capacity is still not sufficient, the section diameter of SMA columns was increased with an increment of 152.4 mm (0.5 ft). The increased column diameter led to a reduction of the axial force ratio a because the gravity load from the superstructures remains the same. The increase in the column weight that slightly increases the load on column section at the base was neglected. The iterations were repeated until the target M_p was reached.

It is worth noting that increasing the diameter will change the stiffness and weight of the column, which is undesirable for practical applications because it will alter the seismic demand of the bridge system. The scope of this research was to understand the M-Phi response of NiTiCo, NiTi and CAM SMA reinforced bridge column sections, and compare their flexural behavior with that of conventional RC columns. Further research is needed to address the dynamic response of the SMA columns and the effect of their lower Young's modulus and possible larger diameter.

4.4 Results and discussion

4.4.1 Sections with different diameters

M-Phi results of RC and SMA columns with different diameters, D, are shown in Figure 4-7. For ease of comparison, the plots in Figure 4-7 are placed vertically. The diameter of RC columns, varying from D = 1219 mm (4 ft), D = 1524 mm (5 ft) and D = 1829 mm (6 ft), were used as the control variable. The reinforcement ratio, r, and axial force ratio, a, of the SMA columns were iterated using the abovementioned method until the idealized plastic moment, M_p, was equivalent to the corresponding RC columns.

The meaning of the annotations in each subfigure of Figure 4-7 is as follows. Take Figure 4-7 (l) for instance: 'NiTiCo-3.1' means the first iteration of NiTiCo column corresponding to 'RC-3'; '#68, max' means it has 68 longitudinal NiTiCo bars, which is the maximum number of bars that can be placed in the section considering the clear spacing limitations; 'F' means the axial force. Because the M_p of 'NiTiCo-3.1' was 26,221 kN-m (19351 kip-ft), less than the target 'RC-3' (M_p = 27,516 kN-m = 20307 kip-ft), a second iteration (labeled as 'NiTiCo-3.2') was performed.

From Figure 4-7 (a) to (c), it is seen that to match M_p with RC-1 (D = 4 ft), the NiTi and CAM columns with a diameter of 4 ft were not strong enough when the maximum number of longitudinal reinforcing bars was reached. The smaller bar diameter and lower yield strength of NiTi and CAM SMA than steel rebar led to the lower M_p of NiTi and CAM SMA column. Therefore, a second iteration with a larger section diameter was needed. When the section diameter was increased to 4.5 ft, the M_p of NiTi and CAM columns was equivalent to RC column and the r was 1.8% and 2.3%, respectively for NiTi and CAM columns.

For the NiTiCo column shown in Figure 4-7 (d), to match the M_p with the RC column, the r of NiTiCo columns was 2.2%, slightly higher than that of the RC (2%). The yield strength of NiTiCo SMA is higher than that of the steel rebar, but it is noted that the diameter of NiTiCo SMA bars (32 mm, 1.26 in) is 3.8 mm (0.15 in) smaller than that of the steel rebar (35.8 mm, 1.41 in). The smaller diameter of SMA bars led to a larger number of bars required for the same plastic moment, thus resulting in a higher r of NiTiCo columns. However, unlike NiTi and CAM columns, the section diameter in the NiTiCo column did not need to be increased due to the higher strength of NiTiCo SMA, indicating the advantage of NiTiCo SMA over the other SMA bars.

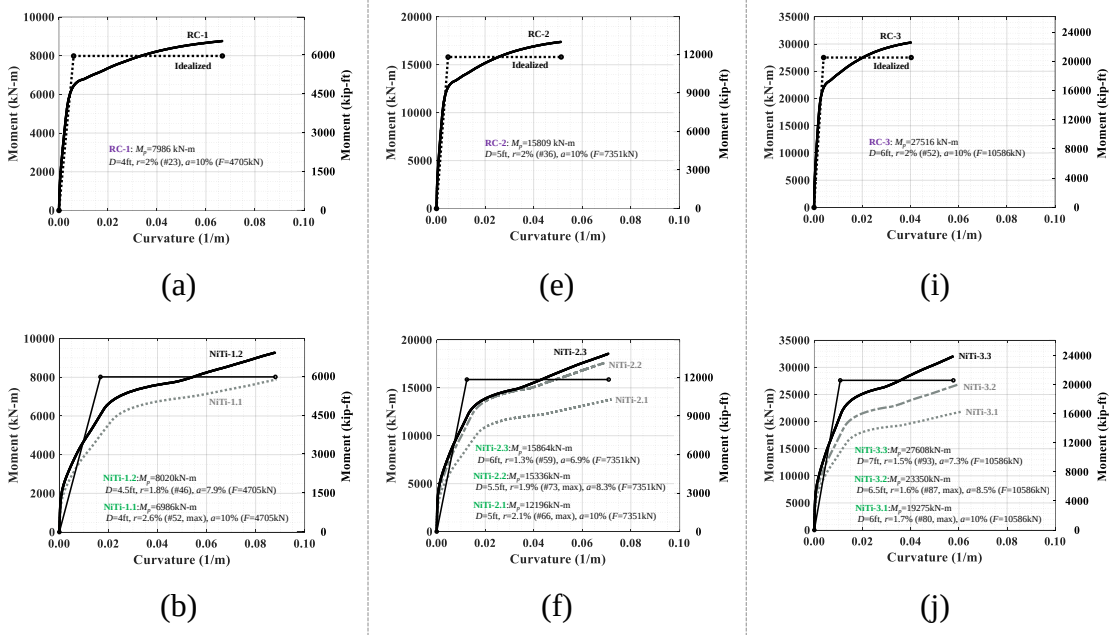

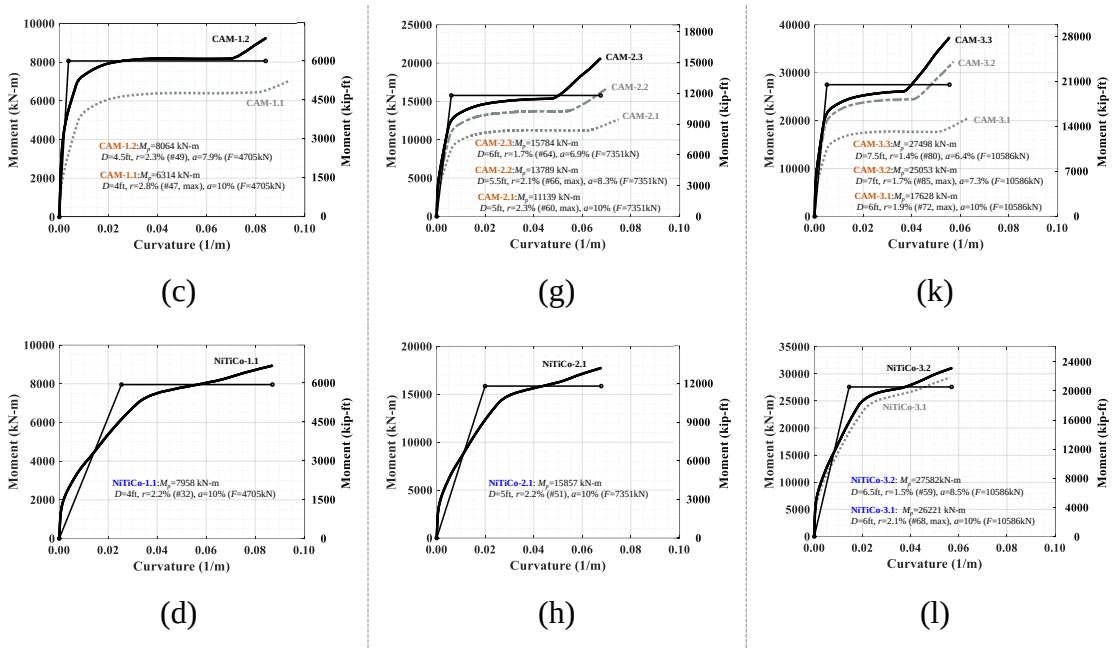

Figure 4-7 M-Phi results of SMA columns matching the RC columns with different section diameter, D: (a) RC-1 with D = 4 ft, (c) to (d) NiTi, CAM and NiTiCo sections iterating to match RC-1; (e) RC-2 with D = 5 ft, (f) to (h) NiTi, CAM and NiTiCo sections iterating to match RC-2; (i) RC-3 with D = 6 ft, (j) to (l) NiTi, CAM and NiTiCo sections iterating to match RC-3.

When increasing the diameter D of RC to 5 ft and 6 ft, as shown in Figure 4-7 (e) to (l), the overall trend in the SMA columns was similar to that shown in Figure 4-7 (a) to (d): when NiTi and CAM columns had the same D as RC, their M_p was smaller than RC columns when the maximum number of longitudinal reinforcements was reached. The diameter in NiTi and CAM sections need to increase by 1 ft or 1.5 ft to match the RC columns M_p. The r of NiTiCo column at D= 5 ft was 2.2%, which was slightly higher than RC-2 with the same M_p. The NiTiCo-3.2, with D= 6.5 ft and r=1.5%, matched the M_p of RC-3, with D= 5 ft and r=2%.

4.4.2 Sections with different reinforcement ratios

M-Phi results of RC and SMA column sections with different reinforcement ratios, *r*, are shown in Figure 4-8. The *r* of RC columns was the control variable assumed to be 1%, 2%, and 3%, and the *D*= 5 ft and *a*= 10%. In Figure 4-8 (a) to (d), RC-4 has an *r* value of 1%. To match M_p of RC-4, *r* had to be increased to 1.6%, 2.1% and 1.1% in NiTi, CAM, and NiTiCo columns, respectively. There was no need to increase the SMA column diameters. In Figure 4-8 (i) to (l), when *r* in RC-4 was increased to 3%, *D* in NiTi, CAM, and NiTiCo columns needed to be increased to match the M_p. Specifically, *D* in NiTi, CAM, and NiTiCo columns needed to be 6.5 ft, 6.5 ft and 5.5 ft; the *r* was reduced to 1.4%, 1.9% and 2.2% in NiTi-6.3, CAM-6.3 and NiTiCo-6.2 , respectively. When the RC columns had a high *r* of 3%, SMA columns needed to have a larger diameter to match the flexural capacity, even for NiTiCo which had a higher yield strength than the steel bars. A similar trend was observed when the longitudinal steel ratio was 2% in the RC section, although the required increase in the SMA section diameter was less than of those matching the plastic moment in the RC column with 3% reinforcement ratio.

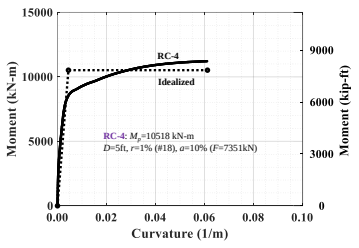

(a)

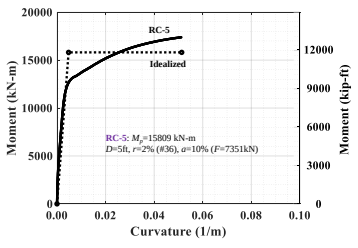

(e)

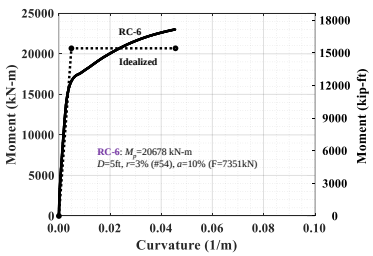

(i)

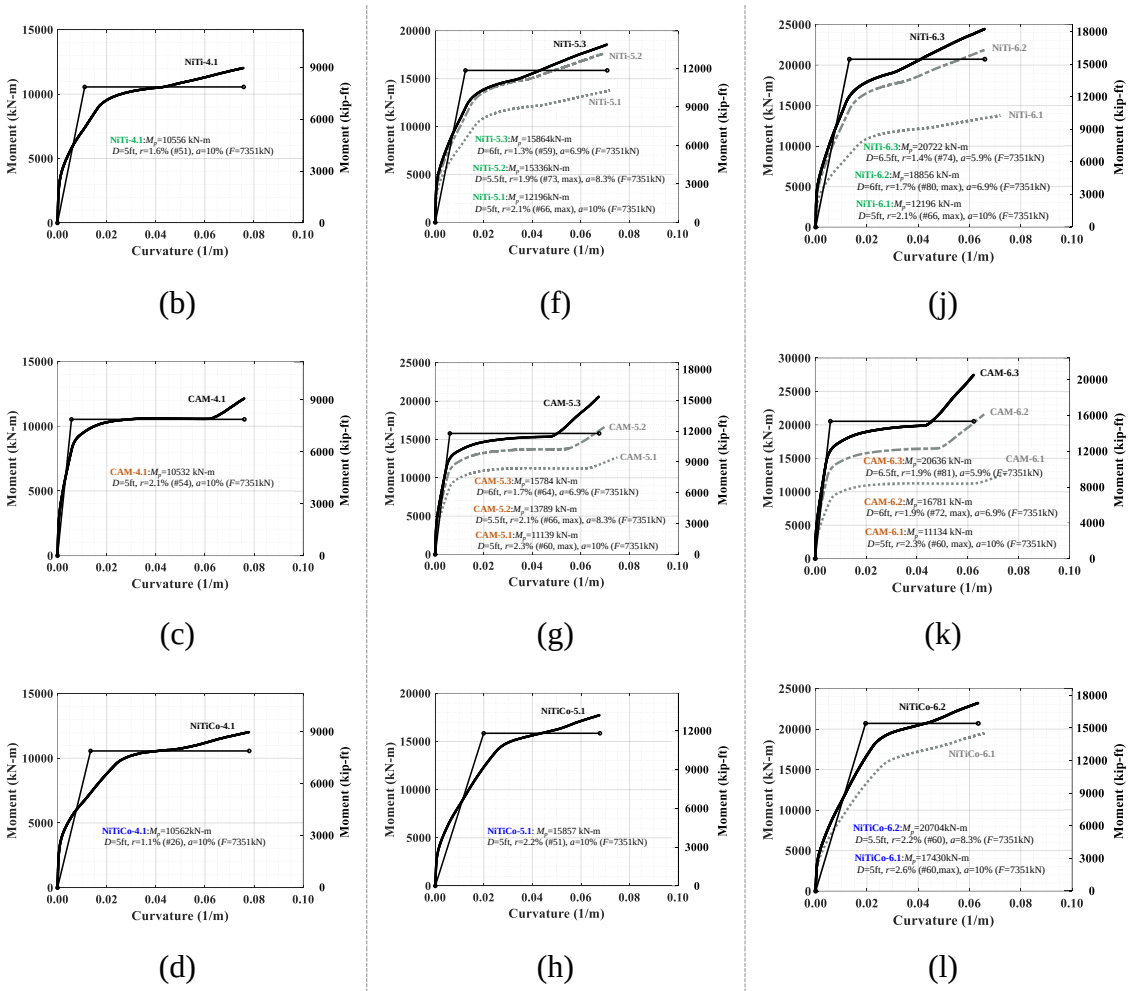

Figure 4-8 M-Phi results of SMA columns matching the RC columns with different reinforcement ratio, *r*: (a) RC-4 with *r* = 1%, (c) to (d) NiTi, CAM and NiTiCo sections iterating to match RC-4; (e) RC-5 with *r* = 2%, (f) to (h) NiTi, CAM and NiTiCo sections iterating to match RC-5; (i) RC-6 with *r* = 3%, (j) to (l) NiTi, CAM and NiTiCo sections iterating to match RC-6.

4.4.3 Sections with different axial force ratios

M-Phi results of RC and SMA columns with different axial force ratios, *a*, are shown in Figure 4-9. The *a* for RC columns was the control variable taken at 5%, 10%, and 15%. The RC section diameter was kept at 5 ft and the longitudinal reinforcement ratio was kept at 2%. Overall, it is seen that as *a* increased, the M_p of RC columns increased and the ultimate curvature reduced, a similar trend was also observed in NiTi, CAM and NiTiCo

columns. This trend is well known. From Figure 4-9 (a) to (d), it is seen that to match the M_p of RC-7 with a= 5%, the D for NiTi and CAM columns needed to be 0.5 ft and 1 ft larger, respectively, reducing r in NiTi-7.2 and CAM-7.3 columns to 1.9%, and 1.7%, respectively. There was no need to increase D for NiTiCo-7.1 to match the M_p of RC-7, but the reinforcement ratio was increased slightly to 2.1%. For RC-9 with a= 15%, the D of NiTi and CAM columns needed to be 1 ft larger; the r of NiTi-9.3 and CAM-7.3 columns was 1.3%, and 1.7%, respectively. Similar to NiTiCo-7.1, D in NiTiCo-8.1, and NiTiCo-9.1 remained at 5 ft, but the reinforcement ratio changed to 2.2% and 2.5%, respectively. The necessary diameter increases in NiTi and CAM sections under 10% axial force ratio were the same as those under 15% ratio.

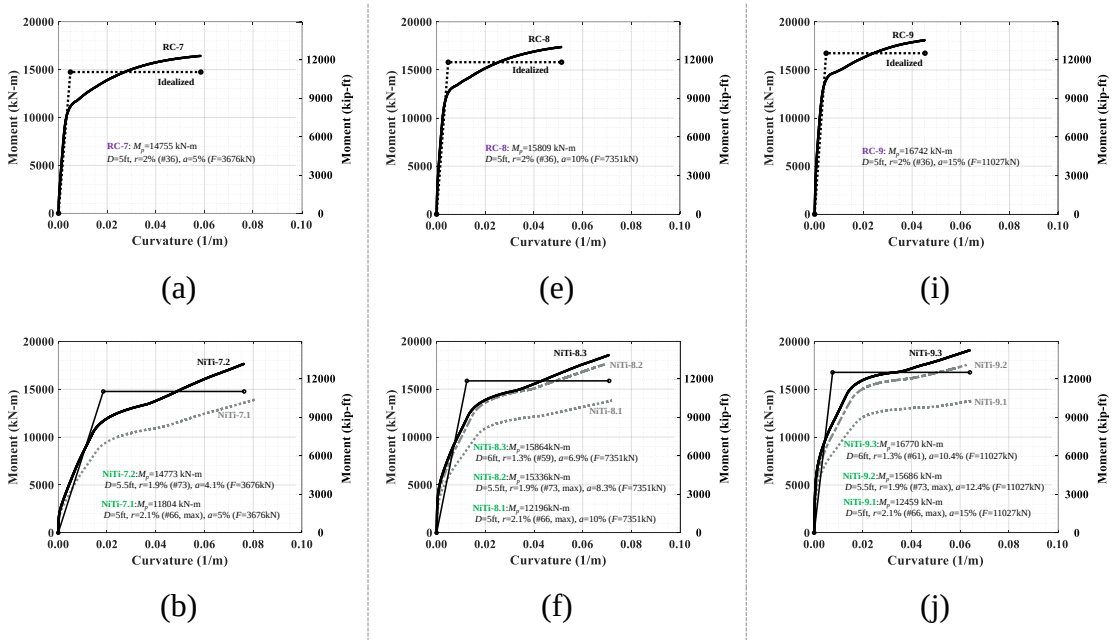

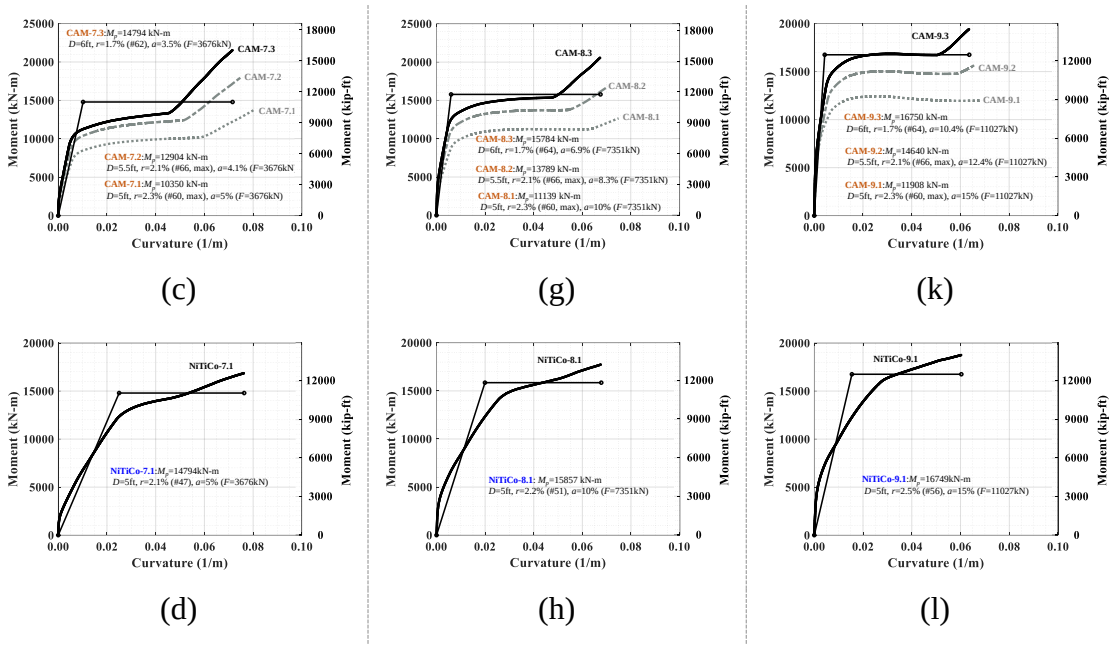

Figure 4-9 M-Phi results of SMA columns matching the RC columns with different axial force ratio, *a*: (a) RC-7 with *a* = 5%, (c) to (d) NiTi, CAM and NiTiCo sections iterating to match RC-7; (e) RC-8 with *a* = 10%, (f) to (h) NiTi, CAM and NiTiCo sections iterating to match RC-8; (i) RC-9 with *a* = 15%, (j) to (l) NiTi, CAM and NiTiCo sections iterating to match RC-8.

4.5 Summary

The criterion to design SMA reinforced column sections that are equivalent to their counterpart RC sections in this study was to match the plastic moment capacity. The moment-curvature analyses results mentioned above are summarized in Table 4-2 to 4. Specifically, Table 4-2 shows the results of sections with different diameters. Table 4-3 shows the results of sections with different longitudinal reinforcement ratios. Table 4-4 shows the results of sections with different axial force ratios. It is noted "(max)" in Table 4-2 to 4 means the maximum number of bars that can be placed in the section considering the clear spacing limitations.

Table 4-2 Sections with different diameters

Column type	Corresponding RC	Column label	Section diameter, *D* (ft)	Longitudinal bar number	Reinforcement ratio, *r*	Axial force, *F* (kip)	Axial force ratio, *a*	*Mp* (kN-m)	*Mp* (kip-ft)
	-	RC-1	4.0	23	2.0%	1069	10.0%	7986	5894

RC column	-	RC-2	5.0	36	2.0%	1671	10.0%	15809	11667
	-	RC-3	6.0	52	2.0%	2406	10.0%	27516	20307
NiTi column	RC-1	NiTi-1.1	4.0	52 (max)	2.6%	1069	10.0%	6986	5156
		NiTi-1.2	4.5	46	1.8%	1069	7.9%	8020	5919
	RC-2	NiTi-2.1	5.0	66 (max)	2.1%	1671	10.0%	12196	9001
		NiTi-2.2	5.5	73 (max)	1.9%	1671	8.3%	15336	11318
		NiTi-2.3	6.0	59	1.3%	1671	6.9%	15864	11708
	RC-3	NiTi-3.1	6.0	80 (max)	1.7%	2406	10.0%	19275	14225
		NiTi-3.2	6.5	87 (max)	1.6%	2406	8.5%	23350	17232
		NiTi-3.3	7.0	93	1.5%	2406	7.3%	27608	20375
CAM column	RC-1	CAM-1.1	4.0	47 (max)	2.8%	1069	10.0%	6314	4660
		CAM-1.2	4.5	49	2.3%	1069	7.9%	8064	5951
	RC-2	CAM-2.1	5.0	60 (max)	2.3%	1671	10.0%	11139	8221
		CAM-2.2	5.5	66 (max)	2.1%	1671	8.3%	13789	10176
		CAM-2.3	6.0	64	1.7%	1671	6.9%	15784	11649
	RC-3	CAM-3.1	6.0	72 (max)	1.9%	2406	10.0%	17628	13009
		CAM-3.2	7.0	85 (max)	1.7%	2406	7.3%	25053	18489
		CAM-3.3	7.5	80	1.4%	2406	6.4%	27498	20294
NiTiCo column	RC-1	NiTiCo-1.1	4.0	32	2.2%	1069	10.0%	7958	5873
	RC-2	NiTiCo-2.1	5.0	51	2.2%	1671	10.0%	15857	11702
	RC-3	NiTiCo-3.1	6.0	68 (max)	2.1%	2406	10.0%	26221	19351
		NiTiCo-3.2	6.5	59	1.5%	2406	8.5%	27582	20356

Table 4-3 Sections with different reinforcement ratios

Column type	Corresponding RC	Column label	Section diameter, *D* (ft)	Longitudinal bar number	Reinforcement ratio, *r*	Axial force, *F* (kip)	Axial force ratio, *a*	*Mp* (kN-m)	*Mp* (kip-ft)
RC column	-	RC-4	5.0	18	1.0%	1671	10.0%	10518	7762
	-	RC-5	5.0	36	2.0%	1671	10.0%	15809	11667
	-	RC-6	5.0	54	3.0%	1671	10.0%	20678	15260

NiTi column	RC-4	NiTi-4.1	5.0	51	1.6%	1671	10.0%	10556	7790
	RC-5	NiTi-5.1	5.0	66 (max)	2.1%	1671	10.0%	12196	9001
		NiTi-5.2	5.5	73 (max)	1.9%	1671	8.3%	15336	11318
		NiTi-5.3	6.0	59	1.3%	1671	6.9%	15864	11708
	RC-6	NiTi-6.1	5.0	66 (max)	2.1%	1671	10.0%	12196	9001
		NiTi-6.2	6.0	80 (max)	1.7%	1671	6.9%	18856	13916
		NiTi-6.3	6.5	74	1.4%	1671	5.9%	20722	15293
CAM column	RC-4	CAM-4.1	5.0	54	2.1%	1671	10.0%	10532	7773
	RC-5	CAM-5.1	5.0	60 (max)	2.3%	1671	10.0%	11139	8221
		CAM-5.2	5.5	66 (max)	2.1%	1671	8.3%	13789	10176
		CAM-5.3	6.0	64	1.7%	1671	6.9%	15784	11649
	RC-6	CAM-6.1	5.0	60 (max)	2.3%	1671	10.0%	11134	8217
		CAM-6.2	6.0	72 (max)	1.9%	1671	6.9%	16781	12384
		CAM-6.3	6.5	81	1.9%	1671	5.9%	20636	15229
NiTiCo column	RC-4	NiTiCo-4.1	5.0	26	1.1%	1671	10.0%	10562	7795
	RC-5	NiTiCo-5.1	5.0	51	2.2%	1671	10.0%	15857	11702
	RC-6	NiTiCo-6.1	5.0	60 (max)	2.6%	1671	10.0%	17430	12863
		NiTiCo-6.2	5.5	60	2.2%	1671	8.3%	20704	15280

Table 4-4 Sections with different axial force ratios

Column type	RC counterpart	Column label	Section diameter, *D* (ft)	Longitudinal bar number	Reinforcement ratio, *r*	Axial force, *F* (kip)	Axial force ratio, *a*	*Mp* (kN-m)	*Mp* (kip-ft)
RC column	-	RC-7	5.0	36	2.0%	835	5.0%	14755	10889
	-	RC-8	5.0	36	2.0%	1671	10.0%	15809	11667
	-	RC-9	5.0	36	2.0%	2506	15.0%	16742	12356
NiTi column	RC-7	NiTi-7.1	5.0	66 (max)	2.1%	835	5.0%	11804	8711
		NiTi-7.2	5.5	73	1.9%	835	4.1%	14773	10902
	RC-8	NiTi-8.1	5.0	66 (max)	2.1%	1671	10.0%	12196	9001
		NiTi-8.2	5.5	73 (max)	1.9%	1671	8.3%	15336	11318
		NiTi-8.3	6.0	59	1.3%	1671	6.9%	15864	11708
	RC-9	NiTi-9.1	5.0	66 (max)	2.1%	2506	15.0%	12459	9195
		NiTi-9.2	5.5	73 (max)	1.9%	2506	12.4%	15686	11576
		NiTi-9.3	6.0	61	1.3%	2506	10.4%	16770	12376
CAM column	RC-7	CAM-7.1	5.0	60 (max)	2.3%	835	5.0%	10350	7638
		CAM-7.2	5.5	66 (max)	2.1%	835	4.1%	12904	9523
		CAM-7.3	6.0	62	1.7%	835	3.5%	14794	10918
	RC-8	CAM-8.1	5.0	60 (max)	2.3%	1671	10.0%	11139	8221

		CAM-8.2	5.5	66 (max)	2.1%	1671	8.3%	13789	10176
		CAM-8.3	6.0	64	1.7%	1671	6.9%	15784	11649
		CAM-9.1	5.0	60 (max)	2.3%	2506	15.0%	11908	8788
	RC-9	CAM-9.2	5.5	66 (max)	2.1%	2506	12.4%	14640	10804
		CAM-9.3	6.0	64	1.7%	2506	10.4%	16750	12362
	RC-7	NiTiCo-7.1	5.0	47 (max)	2.1%	835	5.0%	14794	10918
NiTiCo column	RC-8	NiTiCo-8.1	5.0	51 (max)	2.2%	1671	10.0%	15857	11702
	RC-9	NiTiCo-9.1	5.0	56	2.5%	2506	15.0%	16749	12361

From the above moment-curvature analyses, it was found that due to the yield strength and the Young's modulus of SMA bars are different from those of steel reinforcement, in general the stiffness and plastic moment in SMA reinforced sections are lower than those of reinforced concrete (RC) sections. To match the idealized plastic moment M_p of SMA columns with the RC columns, overall, more SMA bars might be needed that correspond to a higher longitudinal reinforcement ratio, r. Depending on the available SMA bar sizes, the section diameter may have to be increased to maintain sufficient bar spacing. These trends are more likely in Ni-Ti and Cu-Al-Mn columns.

The diameter of Ni-Ti-Co reinforced sections in most cases analyzed in this report remained the same as the RC section diameter due to the higher yield strength of Ni-Ti-Co SMA bars. For example, for the control RC column with section diameter D =5 ft, reinforcement ratio r =2%, and axial force ratio a =10%, to match the M_p of NiTiCo column with the RC column, the r of Ni-Ti-Co columns was 2.2%, slightly higher than that of the RC column (2%). Only when the corresponding RC column had a very large diameter D =6 ft and a very high reinforcement ratio r =3%, the Ni-Ti-Co column diameters needed to be 0.5 ft and 1 ft larger than the corresponding RC column (with D =5 ft, r =2%). In such cases, the r in Ni-Ti-Co column was 1.5% and 2.2%, respectively. Compared with Ni-Ti and Cu-Al-Mn columns, the M_p of Ni-Ti-Co columns were much higher, leading to a much

lower reinforcement ratio and smaller column diameter. All these indicate the advantages of Ni-Ti-Co SMA and the potential of using it in real bridge applications.

CHAPTER 5 SUMMARY AND CONCLUSIONS

5.1 Summary

In this report, the feasibility of using novel iron-based (Fe-Mn-Si) and nickel-titanium-based (Ni-Ti-Co) shape memory alloys (SMAs) in bridge columns to improve extreme event resiliency was investigated. The key material properties of Fe-Mn-Si SMA (FeSMA) and Ni-Ti-Co SMA under seismic loading and possible climatic temperature extremes were characterized and compared with existing SMAs such as Ni-Ti and Cu-Al-Mn alloys. Furthermore, the moment-curvature response of typical bridge columns reinforced with these SMAs was investigated and compared. Specifically, the following research activities were conducted.

For FeSMA, its behavior before (referred to as non-activated FeSMA) and after thermal actuation (referred to as activated FeSMA) was investigated. The strength, ductility, and recovery strain of non-activated FeSMA were investigated by monotonic, and incremental cyclic loading tests at temperatures from -40 °C to 50 °C. The actuation stress degradation, low-cycle fatigue resistance, and deformability of activated FeSMA were investigated by incremental cyclic, low-cycle fatigue, and monotonic loading tests. Prestrain values ranging from 4% to 30%, post-actuation temperatures from -40 °C to 50 °C, and low-cycle fatigue amplitude ranging from 0.5% to 1% were studied.

For Ni-Ti-Co SMA, its superelasticity and low-cycle fatigue resistance were studied experimentally, and its application in typical bridge columns was studied numerically. Incremental cyclic and low-cycle fatigue tests were performed on Ni-Ti-Co SMA at temperatures from -40 °C to 50 °C and compared with Ni-Ti and Cu-Al-Mn SMAs.

Moment-curvature analyses of typical bridge columns reinforced with Ni-Ti-Co SMA were performed and benchmarked against columns reinforced with Ni-Ti and Cu-Al-Mn SMAs, as well as conventional RC columns.

5.2 Conclusions

The main findings from this report were summarized and presented as follows in three parts.

Part I: FeSMA exhibited excellent deformability, cyclic actuation stability, and low-cycle fatigue resistance under a wide range of temperatures from -40 ℃ to 50 ℃ all of which are advantageous for self-centering bridge applications. Specifically, the following conclusions were drawn.

- The fracture strain of non-activated FeSMA at -40 ℃, 23 ℃ and 50 ℃ were all over 25% and the maximum strain reached 58%.
- The yield strength and ultimate strength of non-activated FeSMA increased as the ambient temperature decreased, which is consistent with conventional reinforcing steel.
- The recovery strain of non-activated FeSMA increased with the increasing maximum applied strain or maximum applied stress. For example, the recovery strain at 5% maximum applied strain at -40 ℃, 23 ℃ and 50 ℃ was 0.86%, 0.83% and 0.92%, respectively. When the maximum applied strain was 25%, the recovery strain at -40 ℃, 23 ℃ and 50 ℃ was 1.48%, 1.64% and 1.66%, respectively.

- Increasing the prestrain level effectively increased the post-actuation strain amplitude before the actuation stress reduced to zero. Specifically, at the prestrain levels of 15%, 20% and 25%, the actuation stress decreased to zero when the cyclic loading amplitude reached 1.3%, 1.5% and 1.7%. A 60% to 110% increase compared to the bars prestrained to 4% strain (commonly used in past research). However, in order to avoid the possible fracture of FeSMA bars, a prestrain level of 15% or 20% is suggested for the practical applications.
- Excellent low-cycle fatigue resistance in terms of actuation stress and energy dissipation stability was observed up to 500 cycles. For example, at a fatigue loading amplitude of 0.5% and a prestrain level of 15%, the hysteresis loops of FeSMA remained stable, and the fracture strain after subsequent monotonic loading exceeded 19%.

Part II: Ni-Ti-Co SMA exhibited superelasticity and low-cycle fatigue resistance at temperatures from -40 ℃ to 23 ℃. Furthermore, its strain recovery and energy dissipation capacity at -40℃ was even better than those of Ni-Ti SMA at 0℃, indicating the potential of using Ni-Ti-Co SMA in low temperature applications. At high temperature 50 ℃, the stress-strain curve of Ni-Ti-Co SMA was no longer flag-shaped, but it is worth noting that it still exhibited strain recovery. Specifically, the following conclusions were drawn.

- At room temperature, 23 ℃, the maximum recovery strain of Ni-Ti-Co SMA (around 7%) was close to that of Ni-Ti SMA and smaller than that of Cu-Al-Mn SMA (around 7.6%). The fracture strain of Ni-Ti-Co SMA (around 8%) was lower than that of Ni-Ti SMA (8.5%) and that of Cu-Al-Mn SMA (12.7%).

- At varying temperatures, Ni-Ti-Co SMA exhibited ideal flag-shape stress-strain curves at 23 ℃, 0 ℃, -20 ℃ and -40 ℃. The temperature range in which Ni-Ti-Co SMA showed superelastic response was close to that of Cu-Al-Mn SMA (-40 ℃ to 50 ℃) and wider than that of Ni-Ti SMA (0 ℃ to 50 ℃).

- The superelasticity of Ni-Ti-Co SMA decreased at high temperature 50 ℃: the residual strain started to accumulate at around 3% cyclic strain amplitude. However, it is worth noting that it still exhibited strain recovery: after unloading from 4%, the residual strain was only 0.5%.

- The low-cycle fatigue resistance of Ni-Ti-Co SMA at 23 ℃ was similar to that of Ni-Ti SMA in terms of fatigue life and superelasticity degradation. Both materials fractured after about 100 cycles of 5% constant strain fatigue loading, and neither material had appreciable residual strain accumulation before fracture meaning that the strain recovery capacity throughout the fatigue loading was stable. It is noted that the yield strength and energy dissipation capacity of Ni-Ti-Co SMA decreased faster than those of Ni-Ti SMA.

- Ni-Ti-Co SMA showed excellent fatigue resistance when temperature was reduced to -40℃. The strain recovery and energy dissipation of Ni-Ti-Co SMA at -40℃ was even superior to those of Ni-Ti SMA at 0 ℃. There was no loss of yield strength, energy dissipation, and strain recovery of Ni-Ti-Co SMA during the first 100 cycles of fatigue loading. From 100 to 471 cycles (when the fracture occurred), the strain recovery showed almost no degradation. These characteristics indicate the potential of applying Ni-Ti-Co SMA to bridges in cold regions.

- At 50 ℃, the low-cycle fatigue resistance of Ni-Ti-Co SMA was lower than that at 23 ℃ and lower than that of Ni-Ti SMA at 50 ℃. The hysteresis loops of Ni-Ti-Co at 50 ℃ narrowed within five cycles, leading to a disappearance of the martensitic transformation start and austenitic transformation finish points, as well as a significant decrease in the energy dissipation capacity. It is noted that the strain recovery of Ni-Ti-Co at 50 ℃ had no degradation during the fatigue loading.

- It is worth noting that most of the Ni-Ti-Co and Ni-Ti SMA samples tested in this study fractured at the thread ends due to stress concentrations. That means that the true fracture strain and low-cycle fatigue life of these two materials are larger than the reported values, which needs further investigation.

Part III: When applied in typical bridge columns, the Ni-Ti-Co SMA reinforced sections overall had comparable flexural capacity to conventional RC columns. Compared with Ni-Ti and Cu-Al-Mn SMAs reinforced sections, the flexural capacity of Ni-Ti-Co SMA reinforced section had lower longitudinal reinforcement ratio and smaller section diameter due to the higher yield strength of Ni-Ti-Co SMA. All these indicate the advantages of Ni-Ti-Co SMA and the potential of using it in real bridge applications. Specifically, the following conclusions were drawn.

- Because the yield strength and the Young's modulus of SMA bars are different from those of steel reinforcement, in general the stiffness and plastic moment in SMA reinforced sections are lower than those of RC sections. To match the idealized plastic moment of SMA columns with the RC columns, overall, more SMA bars might be needed that correspond to a higher longitudinal

reinforcement ratio. Depending on the available SMA bar sizes, the section diameter may have to be increased to maintain sufficient bar spacing. These trends are more likely in the Ni-Ti and Cu-Al-Mn columns.

- The diameter of Ni-Ti-Co reinforced sections in most cases analyzed in this report remained the same as the RC section diameter due to the higher yield strength of Ni-Ti-Co SMA bars. Compared with Ni-Ti and Cu-Al-Mn columns, the idealized plastic moment of Ni-Ti-Co columns was much higher, leading to a much lower reinforcement ratio and smaller column diameter.

5.3 Recommendations for future research

FeSMA and Ni-Ti-Co SMA have proven to be feasible for use in real bridge columns subjected to seismic loading and extreme climatic temperatures. Based on the findings from this report, future research needs are listed as follows.

- Whether FeSMA exhibits a lower ductility at room temperature than that at high or low temperatures should be further investigated.
- The fracture toughness of Ni-Ti-Co SMA at different temperatures in comparison with Ni-Ti and Cu-Al-Mn SMAs should be investigated.
- The seismic performance of full-scale bridge columns post-tensioned with FeSMA bars should be investigated to further understand the application of FeSMA bars at the structural level.
- The structural performance of full-scale bridge columns reinforced with Ni-Ti-Co SMA bars should be investigated and compared with columns reinforced with conventional Ni-Ti SMAs from previous research.

- The reliable connection method between large size Ni-Ti-Co SMA and steel rebar should be investigated to further facilitate the application of Ni-Ti-Co SMA in bridges.

This study was the first phase of a broader study with the ultimate goal of determining alternative, cost-effective SMAs for application in bridges. The seismic performance of bridge columns reinforced with FeSMA and Ni-Ti-Co SMA at the structural level will be conducted in the second phase of this project.

ACKNOWLEDGMENTS

The author would like to thank SAES Smart Materials for providing the Ni-Ti-Co and Ni-Ti materials, Re-fer AG. for providing the Fe-Mn-Si material, and Furukawa Techno Material Co., LTD. for providing the Cu-Al-Mn material. Any opinions, findings, conclusions, or recommendations are those of the author and do not necessarily reflect the views of the funding agency.

REFERENCES

AASHTO. 2011. “Guide Specifications for LRFD Seismic Bridge Design.” *Am. Assoc. State Highw. Transp. Off.*

ASTM E8/E8M. 2013. “Standard Test Methods for Tension Testing of Metallic Materials.” *West Conshohocken, PA, USA.* https://doi.org/10.1520/E0008_E0008M-13A.

Cladera, A., L. A. Montoya-Coronado, J. G. Ruiz-Pinilla, and C. Ribas. 2020. “Shear strengthening of slender reinforced concrete T-shaped beams using iron-based shape memory alloy strips.” *Eng. Struct.*, 221: 111018. https://doi.org/10.1016/j.engstruct.2020.111018.

Cladera, A., B. Weber, C. Leinenbach, C. Czaderski, M. Shahverdi, and M. Motavalli. 2014. “Iron-based shape memory alloys for civil engineering structures: An overview.” *Constr. Build. Mater.*, 63: 281–293. https://doi.org/10.1016/j.conbuildmat.2014.04.032.

Czaderski, C., M. Shahverdi, and J. Michels. 2021. “Iron based shape memory alloys as shear reinforcement for bridge girders.” *Constr. Build. Mater.*, 274: 121793. https://doi.org/10.1016/j.conbuildmat.2020.121793.

Fasching, A., D. Norwich, T. Geiser, and G. W. Paul. 2011. “An evaluation of a NiTiCo alloy and its suitability for medical device applications.” *J. Mater. Eng. Perform.*, 641–645.

Gencturk, B., Y. Araki, T. Kusama, T. Omori, R. Kainuma, and F. Medina. 2014. “Loading rate and temperature dependency of superelastic Cu-Al-Mn alloys.” *Constr. Build. Mater.*, 53: 555–560. https://doi.org/10.1016/j.conbuildmat.2013.12.002.

Gencturk, B., and M. S. Saiidi. 2022. “Material Characteristics of Cu-Based Superelastic Alloys for Applications in Bridge Columns to Improve Seismic

Performance.” *NCHRP-IDEA-Project-210. Progr. Proj. Final Rep.*

Hong, H., B. Gencturk, Y. Araki, S. Saiidi, and S. Kise. 2024a. “Machinability of Cu-Al-Mn Shape Memory Alloys.” *J. Mater. Civ. Eng.*, 36 (7): 04024188. https://doi.org/10.1061/JMCEE7.MTENG-17497.

Hong, H., B. Gencturk, H. Aryan, A. Jain, Y. Araki, M. S. Saiidi, and S. Kise. 2022a. “Low-cycle fatigue behavior of Cu–Al–Mn superelastic alloys at different temperatures.” *Smart Mater. Struct.*, 31 (11): 115022. https://doi.org/10.1088/1361-665X/ac97d3.

Hong, H., B. Gencturk, S. A. Brown, F. Hosseini, A. Jain, H. Aryan, S. Saiidi, Y. Araki, and S. Kise. 2022b. “Long-term corrosion resistance of Cu-Al-Mn superelastic alloys and steel rebar for use in bridges.” *Constr. Build. Mater.*, 350: 128795. https://doi.org/10.1016/j.conbuildmat.2022.128795.

Hong, H., B. Gencturk, S. Kise, Y. Araki, A. Jain, S. Saiidi, and K. Uruma. 2024b. “Headed Coupling Behavior of Large Diameter Cu-Al-Mn Shape Memory Alloy Bars: Mechanical Testing and Microstructural Analyses.” *Constr. Build. Mater.*, 424: 135862. https://doi.org/10.1016/j.conbuildmat.2024.135862.

Kise, S., Y. Araki, T. Omori, and R. Kainuma. 2021. “Orientation Dependence of Plasticity and Fracture in Single-Crystal Superelastic Cu-Al-Mn SMA Bars.” *J. Mater. Civ. Eng.*, 33 (4): 04021027. https://doi.org/10.1061/(asce)mt.1943-5533.0003568.

Kishi, Y., Z. Yajima, and K. Shimizu. 2002. “Relation between tensile deformation behavior and microstructure in a Ti-Ni-Co shape memory alloy.” *Mater. Trans.*, 43 (5): 834–839. https://doi.org/10.2320/matertrans.43.834.

Lee, W. J., B. Weber, G. Feltrin, C. Czaderski, M. Motavalli, and C. Leinenbach. 2013. “Stress recovery behaviour of an Fe–Mn–Si–Cr–Ni–VC shape memory alloy used for prestressing.” *Smart Mater. Struct.*, 22 (12): 125037.

https://doi.org/10.1088/0964-1726/22/12/125037.

Ma, D. Y., L. H. Han, X. L. Zhao, and W. B. Yang. 2020. “Seismic performance of the concrete-encased CFST column to RC beam joints: Analytical study.” *Steel Compos. Struct.*, 36 (5). https://doi.org/10.12989/scs.2020.36.5.533.

Mander, J. B., M. J. N. Priestley, and R. Park. 1988. “Theoretical Stress-Strain Model for Confined Concrete.” *J. Struct. Eng.*, 114 (8). https://doi.org/10.1061/(ASCE)0733-9445(1988)114:8(1804).

Manjeri, R. M., D. Norwich, F. Sczerzenie, X. Huang, M. Long, and M. Ehrlinspiel. 2016. “A Study of Thermo-mechanically Processed High Stiffness NiTiCo Shape Memory Alloy.” *J. Mater. Eng. Perform.*, 25 (3): 894–900. https://doi.org/10.1007/s11665-016-1932-8.

Montejo, L. A., J. E. Sloan, M. J. Kowalsky, and T. Hassan. 2008. “Cyclic Response of Reinforced Concrete Members at Low Temperatures.” *J. Cold Reg. Eng.*, 22 (3): 79–102. https://doi.org/10.1061/(asce)0887-381x(2008)22:3(79).

Motaref, S. 2011a. “Seismic Response of Precast Bridge Columns with Energy Dissipating Joints.” *Univ. Nevada, Reno*, Dissertation.

Motaref, S. 2011b. “Seismic Response of Precast Bridge Columns with Energy Dissipating Joints.” *Univ. Nevada, Reno*. https://doi.org/Dissertation.

Omori, T., S. Kawata, and R. Kainuma. 2020. “Orientation dependence of superelasticity and stress hysteresis in Cu-Al-Mn alloy.” *Mater. Trans.*, 61 (1): 55–60. https://doi.org/10.2320/matertrans.MT-MJ2019008.

PEER. 2000. “Open System for Earthquake Engineering Simulation (OpenSees).” *Univ. California, Berkeley, CA*.

Pulido, C., M. Saiid Saiidi, D. Sanders, A. Itani, and S. El-Azazy. 2004. “Seismic performance of two-column bents - Part I: Retrofit with carbon fiber-

reinforced polymer fabrics." *ACI Struct. J.*, 101 (4): 558–568. https://doi.org/10.14359/13342.

Raza, S., R. Widmann, J. Michels, M. Saiid Saiidi, M. Motavalli, and M. Shahverdi. 2023. "Self-centering technique for existing concrete bridge columns using prestressed iron-based shape memory alloy reinforcement." *Eng. Struct.*, 294: 116799. https://doi.org/10.1016/j.engstruct.2023.116799.

Saiidi, M. S., M. O'Brien, and S. Z. Mahmoud. 2009. "Cyclic response of concrete bridge columns using superelastic nitinol and bendable concrete." *ACI Struct. J.*, 106 (1): 69–77. https://doi.org/10.14359/56285.

Schoettler, Restrepo, Guerrini, D. C. 2015. "A Full-Scale, Single-Column Bridge Bent Tested by Shake-Table Excitation." *PEER Rep. No. 2015/02*, Pacific Earthquake Engineering Research Center.

Schranz, B., J. Michels, C. Czaderski, M. Motavalli, T. Vogel, and M. Shahverdi. 2021. "Strengthening and prestressing of bridge decks with ribbed iron-based shape memory alloy bars." *Eng. Struct.*, 241: 112467. https://doi.org/10.1016/j.engstruct.2021.112467.

Shahverdi, M., J. Michels, C. Czaderski, and M. Motavalli. 2018. "Iron-based shape memory alloy strips for strengthening RC members: Material behavior and characterization." *Constr. Build. Mater.*, 173: 586–599. https://doi.org/10.1016/j.conbuildmat.2018.04.057.

Shrestha, K. C., Y. Araki, T. Kusama, T. Omori, and R. Kainuma. 2016. "Functional Fatigue of Polycrystalline Cu-Al-Mn Superelastic Alloy Bars under Cyclic Tension." *J. Mater. Civ. Eng.*, 28 (5): 4015194. https://doi.org/10.1061/(asce)mt.1943-5533.0001417.

Tazarv, M. 2014. "Next Generation of Bridge Columns for Accelerated Bridge Construction in High Seismic Zones." *Univ. Nevada, Reno*.

Tazarv, M., and M. Saiidi. 2015. "Low-Damage Precast Columns for Accelerated

Bridge Construction in High Seismic Zones." *J. Bridg. Eng.,* 21: 4015056. https://doi.org/10.1061/(ASCE)BE.1943-5592.0000806.

Vůjtěch, J., P. Ryjáček, J. Campos Matos, and E. Ghafoori. 2021. "Iron-Based shape memory alloy for strengthening of 113-Year bridge." *Eng. Struct.,* 248: 113231. https://doi.org/10.1016/j.engstruct.2021.113231.

Yan, J. B., J. Cao, P. Xie, and J. Xie. 2023. "Concrete-filled circular stainless-steel tubular columns subjected to low-temperature axial compression." *Structures,* 55: 916–932. https://doi.org/10.1016/j.istruc.2023.06.054.

Youssf, O., M. A. ElGawady, and J. E. Mills. 2015. "Experimental Investigation of Crumb Rubber Concrete Columns under Seismic Loading." *Structures,* 3: 13–27. https://doi.org/10.1016/j.istruc.2015.02.005.

Zhang, Y., J. A. Camilleri, and S. Zhu. 2008. "Mechanical properties of superelastic Cu-Al-Be wires at cold temperatures for the seismic protection of bridges." *Smart Mater. Struct.,* 17 (2): 025008. https://doi.org/10.1088/0964-1726/17/2/025008.